

Surface enzyme-polymerization endows Janus hydrogel tough adhesion and regenerative repair in penetrating orocutaneous fistulas

Received: 25 April 2024

Accepted: 5 December 2024

Published online: 30 December 2024

 Check for updates

Ye Ju^{1,5}, Chunyue Ma ^{2,3,5}, Ling Ding^{4,5}, Mingyue Shi⁴, Xia Wang⁴, Dongbei Wu⁴, Qing Wu¹ , Xingjun Qin ²  & Qigang Wang ^{1,4} 

Penetrating orocutaneous or oropharyngeal fistulas (POFs), severe complications following unsuccessful oral or oropharyngeal reconstruction, remain complex clinical challenges due to lack of supportive tissue, contamination with saliva and chewed food, and dynamic oral environment. Here, we present a Janus hydrogel adhesive (JHA) with asymmetric functions on opposite sides fabricated via a facile surface enzyme-initiated polymerization (SEIP) approach, which self-entrap surface water and blood within an in-situ formed hydrogel layer (RL) to effectively bridge biological tissues with a supporting hydrogel (SL), achieving superior wet-adhesion and seamless wound plugging. The tough SL hydrogel interlocked with RL dissipates energy to withstand external mechanical stimuli from continuous oral motions like chewing and swallowing, thus reducing stress-induced damage. In male New Zealand rabbit POF models, the JHA demonstrates strong adhesion and fluid-tight sealing, and maintained firm sealing for over 3 days without any decreased signs under a normal diet. After 12 days, both extraoral cutaneous and mucosal wounds achieved complete closure, with mechanical strengths comparable to normal tissues. Similar therapeutic efficacy was also confirmed in male beagle dog POF models. Thus, the proposed JHA hydrogel shows great potential for deep wound sealing and providing mechanical support to assist healing in penetrating fistulas and other injuries.

Penetrating orocutaneous or oropharyngeal fistulas (POFs), severe complications following unsuccessful oral or oropharyngeal reconstruction, frequently occur in the oral and maxillofacial region with an incidence ranging from 9% to 30%¹. The POFs can be classified into

simple types (traumatic, surgical, infectious) and complicated types (irradiated, diabetic, vascular-disease related) based on various causes, significantly impacting patients' mental well-being and quality of life. Unlike cutaneous wounds, POFs are typically challenged by the highly

¹Shanghai Key Laboratory of Anesthesiology and Brain Functional Modulation, Clinical Research Center for Anesthesiology and Perioperative Medicine, Translational Research Institute of Brain and Brain-Like Intelligence, Shanghai Fourth People's Hospital, School of Medicine, Tongji University, Shanghai, China. ²Department of Oral Maxillofacial-Head and Neck Oncology, Shanghai Ninth People's Hospital, Shanghai Jiao Tong University School of Medicine; College of Stomatology, Shanghai Jiao Tong University; National Center for Stomatology; National Clinical Research Center for Oral Diseases; Shanghai Key Laboratory of Stomatology, Shanghai, China. ³Department of Oral and Maxillofacial Surgery, Hainan Western Central Hospital, Dan Zhou, China. ⁴School of Chemical Science and Engineering, Tongji University, Shanghai, China. ⁵These authors contributed equally: Ye Ju, Chunyue Ma, Ling Ding.

 e-mail: 2305045@tongji.edu.cn; qinxj112064@sh9hospital.org.cn; wangqg66@tongji.edu.cn

moist environment of the mouth or pharynx, continuous saliva output, contamination from food intake, as well as repeated mechanical stimuli generated by physiological actions such as speech and swallowing, making their clinical treatments particularly difficult and intractable². The routine conservative clinical interventions for POFs are largely centered on iodoform or Dakin's solution followed by normal saline dressings, and negative pressure wound therapy (NPWT)^{3–5}. However, these temporary dressings need to be changed frequently and are often far from satisfactory for effective wound sealing, likely leading to bacterial accumulation, persistent inflammation and delayed wound healing. Additionally, the use of NPWT requires restrictions on patient movement, and nasogastric tubes or gastrotomy may be necessary sometimes, further complicating the management process. If failure occurs, surgical interventions such as adjacent tissue rotation and flap reconstruction may be needed; however, these methods are complex, costly, and often poorly tolerated by patients⁶. Therefore, it is imperative to develop alternative therapeutic strategies for POFs treatment.

Hydrogel adhesives have gained considerable attention for wound sealing and promoting tissue healing, providing promising candidates to seal the penetrating fistulas and support their regeneration^{7–10}. The keys to achieving robust adhesion with wet tissues are focused on breaking down the hydration layer and creating strong interactions with tissue surface^{11–13}. One promising approach involves the use of water-absorbing materials, such as hydrophilic polymers, to remove the interfacial water and establish an effective reaction surface^{14–16}. As a pioneering example, Zhao and coworkers developed a dry double-sided tape (DST) by combining a biopolymer such as gelatin, poly-acrylic acid grafted with NHS ester (PAA-NHS ester), and acrylic monomer¹⁴. This wet-adhesive mechanism primarily relies on the quick absorption of interfacial water through the swelling of the dried DST film, resulting in physical interactions with the tissue surface, such as hydrogen bonding and electrostatic interactions, to offer a rapid temporary adhesion. Subsequently, covalent crosslinks were formed between the NHS active esters and amine groups on the tissue surface, thus achieving tough and lasting adhesion to diverse wet tissues. Alternatively, another representative method employs phase separation and increased hydrophobicity of the polymer to repel the interfacial water, leading to sufficient contact interface and enhanced non-covalent interaction with the adherent substrate^{17–19}. For example, Liu and co-workers synthesized a hyperbranched polymer (HBP) with a hydrophobic backbone and hydrophilic adhesive catechol side branches, where the hydrophobic chains rapidly self-aggregate to form coacervates upon contact with water, immediately displacing surface hydrated water and exposing more reactive catechol groups for bonding, thus enabling strong adhesion in aqueous environments¹⁷. Despite such progress, these hydrogel adhesives still struggle to achieve a satisfactory balance in meeting the multi-functional requirements for POFs treatment. To the best of our knowledge, there is no relevant research concerning the design of reliable hydrogel adhesives specifically for POFs sealing and accelerating regeneration.

Given the evolving pathological environment and complex anatomical structure of the oral cavity and oropharynx, ideal repairing materials should not only offer reliable barrier protection with strong adhesive sealing against intraoral irritants and regeneration-promoting benefits, but should also ensure long-term mechanical tolerance to withstand repeated oral actions like chewing and swallowing. These concerns are reminiscent of Janus hydrogel adhesives, which feature asymmetric properties and distinct functions on opposite sides^{10,20–22}, providing a promising solution to address the above-mentioned challenges in the treatment of highly complicated POF wounds. In our previous works, we developed a series of oxidoreductase-mediated gelation methods triggered by physiological substances (such as blood glucose, hemoglobin), for the biomimetic

formation of enzyme-laden hydrogels with favorable biocompatibilities, which created opportunities to engineer Janus hydrogels anchoring on wound surfaces for fistulas sealing in a tissue-compatible way^{23–25}. In addition, compared to enzyme-polymer conjugates that involve chemical bonding, this self-confined enzyme-immobilization process akin to physical entrapment can attain enhanced catalytic activity and stability by adjusting the monomer's molecular weight and the polymerization degree, ensuring efficient enzyme-catalyzed induced modulation of regenerative microenvironments to accelerate wounds healing^{26–28}.

Herein, we propose a class of in-situ growing Janus hydrogel adhesive (JHA) constructed by the wound surface enzyme-initiated polymerization (SEIP) approach, which creates a new hydrogel layer (RL) between the wound surface and a tough supporting layer hydrogel (SL) triggered by blood glucose, resulting in seamless plugging of the penetrating wounds (Fig. 1). The surface blood and water are self-confined as components within the in-situ formed RL hydrogel, effectively counteracting their detrimental effects on the wet interface. Accompanied by the in-situ gelation process, the interfacial bonding of tissue is achieved through the formation of covalent bonds via NHS-amino reaction, which is a molecular-level interfacial interaction, leading to strong adhesion with wet tissues. The tough SL hydrogel effectively interlocks with RL hydrogel, providing energy dissipation to withstand external mechanical stimuli from continuous oral motions such as chewing and swallowing, thus efficiently reducing the stress-induced damage. In addition, the soft RL hydrogel also facilitates wound closure and tissue regeneration by creating a favorable regenerative microenvironment conducive to cell growth. Both on New Zealand rabbit and Beagle dog POF models, the proposed JHA demonstrated tough adhesion and fluid-tight sealing, as well as excellent therapeutic efficacy with full re-epithelialization observed in both buccal skin and mucosa. We believe that the JHA with ingenious modular architecture provides potential clinical opportunities for POFs treatment, as well as other leak-related defects such as intestinal fistulas and anal fistulas.

Results

Surface enzyme-initiated gelation mechanism and characterization of JHA

The JHA was prepared from a prefabricated SL and an in-situ gelation of an RL through surface enzyme-initiated polymerization (SEIP). Typically, as illustrated in Fig. 1b, a tough xerogel served as the mechanical supporting layer (SL) was modified with GOx on the surface, which captures glucose from the blood once direct contact with the wound surface with pressure, catalyzing the conversion of glucose and O₂ into gluconic acid and H₂O₂. The generated H₂O₂ then reacts with Fe[Gly]₂ in the surface precursor to initiate the enzymatic cascade by internalizing the glycine ligand to produce carbon radicals, thus triggering the interfacial radical polymerization, leading to the fast generation of a new hydrogel layer (namely RL) on SL surface and the in-situ preparation of JHA on tissue surface. The backbone structure of the tough SL was polyacrylic acid (PAA) networks, with long-chain glycidyl methacrylate-modified chondroitin sulfate (CSMA) as the cross-linking agent and encapsulated chondroitin sulfate (CS), which endowed the JHA with strong mechanical properties for effectively dissipating energy under deformation. The RL should not only be biocompatible and suitable for cell proliferation and tissue regeneration but also adhere stably to the tissue to comply with the dynamic movement of tissue. To satisfy the RL criterion, we employed biocompatible CSMA as the main component. The obtained CSMA was elucidated by ¹H nuclear magnetic resonance (NMR) (Fig. S1). Moreover, small amounts of N,N-dimethylacetamide (DMAA) and N-succinimidyl acrylate (AAC-NHS) were added to adjust the mechanical and adhesion properties of the RL. AAC-NHS enables the hydrogel to covalently bond with primary amino groups

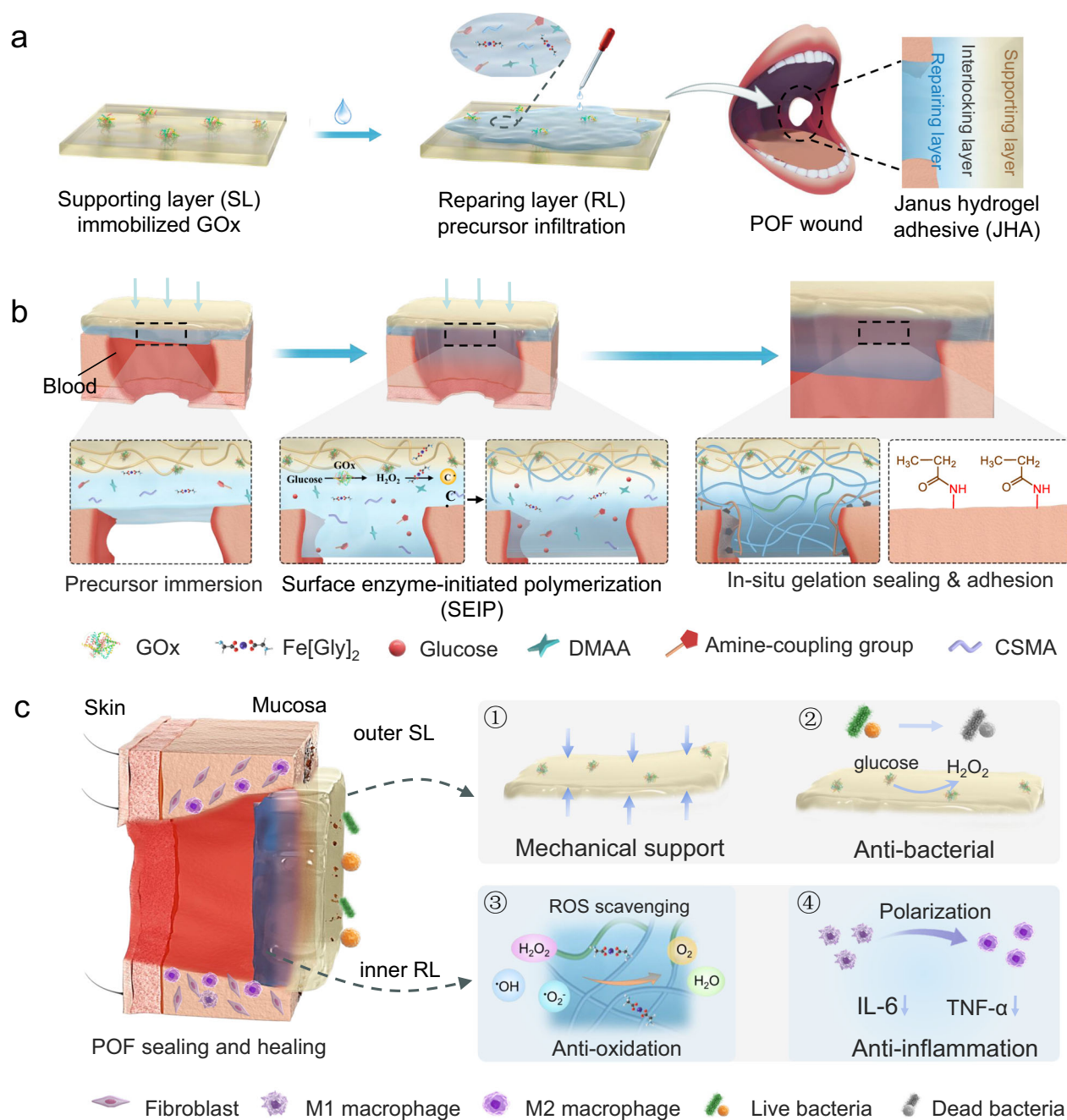


Fig. 1 | Integration and repair mechanism of JHA and its application scope.

a Schematic illustration of the preparation procedures to construct JHA. **b** The process of SEIP to form JHA in situ: surface-immobilized GOx on the SL catalyze the blood glucose and O₂ into gluconic acid and H₂O₂, which combined with ferrous glycinate (Fe[Gly]₂) in the surface precursor to generate carbon radicals for initiating the interfacial radical polymerization, thus resulting in the fast generation of RL on the tissue surface; accompanied by the gelation process, the N-succinimidyl

acrylate (AAc-NHS) in the RL precursor reacts with the amino groups on tissue surface, forming strong interfacial covalent bonding with the tissue, thereby enabling robust wet-adhesion and wound sealing. **c** The application of JHA for promoting POF wound healing by adhering JHA to tissue surfaces for sealing the penetrating wound and protecting it from mechanical stimuli and bacterial infection, relieving oxidative stress and creating a pro-healing microenvironment.

on the surface of tissue to achieve stable and robust adhesion with wet biological tissues.

The SL should be well-matched to biological tissues in a dynamic physiological environment. As shown in Fig. 2a, the PAA hydrogel exhibited a breaking elongation of more than 2800%. In addition, the hydrogel exhibited good elasticity and stability during loading-unloading cycles at varying elongations and constant elongations (Fig. 2b and Fig. S2a), and after the first stretch, the energy dissipation remained stable (Fig. S2b). Puncture tests (Fig. 2c) revealed that the puncture strength of the hydrogel reached more than 1MPa and that

the hydrogel withstood more than 5600% puncture strain. Analogous to the tensile breaking energy in the tensile test, we propose the concept of puncture energy, that is, the energy required for a fine needle per unit volume to completely pierce the polymer film. By integrating the puncture stress-strain curve, it was concluded that the puncture energy of the hydrogel reached 22.99 MJ/m³. All of the above mechanical tests indicate that the SL hydrogel possesses the expected mechanical stability and ability to resist damage from external forces. This is mainly due to the hard three-dimensional polymer network and the multiple noncovalent interactions between polyacrylic acid and

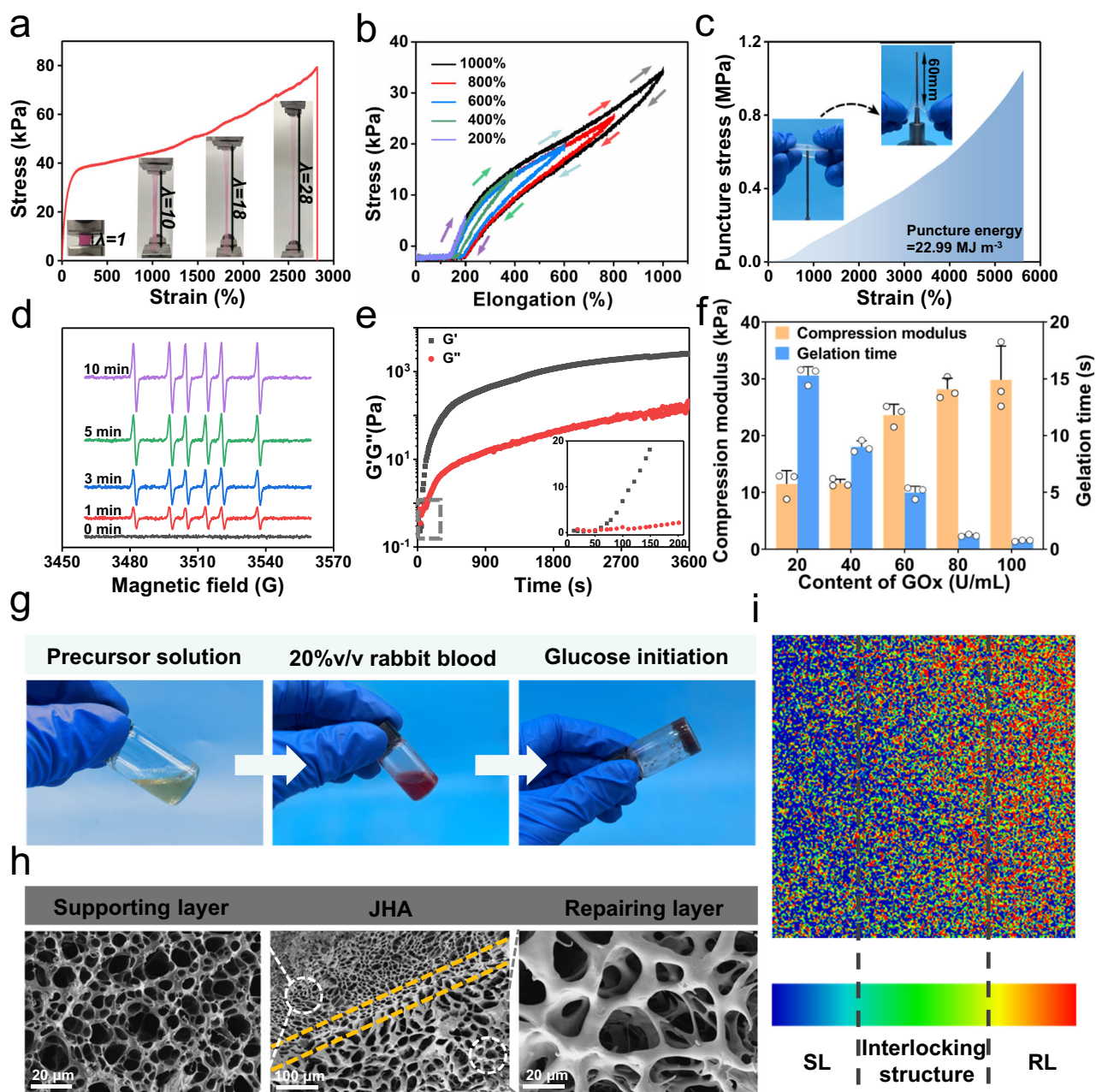


Fig. 2 | Performance characterization of JHA. **a** Tensile stress-strain curve of the SL hydrogel. **b** Load-unload curves with various elongations. **c** Puncture stress-strain curve of the SL hydrogel. **d** EPR spectra of carbon radicals generated by GOx/Fe[Gly]₂/Glu at different times. **e** Curves of the storage modulus (G') and loss modulus (G'') of the RL hydrogel in oscillation time sweep mode at 37 °C. **f** Gelation

time and compressive modulus of the hydrogels induced by different concentrations of GOx. Data are shown as mean \pm standard deviation (s.d.) ($n = 3$ independent samples). **g** Schematic diagram of the rapid gelation of the RL hydrogel in blood. **h** SEM spectrum of the JHA. **i** Raman mapping at 2936 cm^{-1} for the section of JHA.

polysaccharides that act as sacrificial bonds, which could effectively dissipate the energy in the deformation process.

The RL hydrogel was rapidly formed by SL-surface GOx catalytic polymerization with glucose and Fe[Gly]₂ in the precursor solution. The cascade catalytic mechanism of GOx/Fe[Gly]₂ indicates that Fe[Gly]₂ decomposes under the action of H₂O₂ produced by GOx and glucose to form carbon free radicals via peroxidation and decarboxylation to initiate free radical polymerization. The EPR spectrum demonstrated that the DMPO-C signal (spin height ratio: 1:1:1:1:1: sextet, $aN = 1.49$ mT, $aH = 2.29$ mT, $g = 2.001$) in the catalytic reaction could be observed with DMPO as the capture agent (Fig. 2d). The storage modulus (G') and loss modulus (G'') curves of the system in the 37 °C oscillation time sweep mode are shown in Fig. 2e. The $G'G''$

curves intersected within 60 s, which showed that the system could rapidly form a gel in a short time. In addition, the storage modulus remained stable with a scanning frequency of 10–0.1 Hz, suggesting the excellent mechanical properties of the final RL hydrogel (Fig. S3). It is worth noting that the gelation rate and mechanical strength of RL hydrogel could be subtly adjusted by the GOx concentration. Under the condition of a constant glucose concentration, the mechanical properties (Fig. S4) and gelation time of the RL, which was formed by GOx-initiated polymerization with varying GOx concentrations, were analyzed. As shown in Fig. 2f and Table S1, the gelation time of RL hydrogel decreased with the increasing of GOx concentration, and the RL could even be formed within 1 s when the concentration of GOx was 100 U/mL. As the gelation accelerated, the compressive modulus of

the hydrogel increased from 9.7 kPa to 30.0 kPa (Fig. 2f), which may have been due to faster gelation resulting in a higher crosslinking density and stronger hydrogel mechanical properties. In view of the complicated composition of body fluid, 20% (v/v) New Zealand rabbit blood was added to the precursor solution to simulate the gelation behaviors at the wound site. As shown in Fig. 2g, the hydrogel formed within 5 min under these conditions. Therefore, the rapid prototyping of RL under physiological conditions can ensure the in situ formation of JHA to achieve seamless plugging of irregular POFs.

The microscopic morphology of the JHA was observed through scanning electron microscopy (SEM) images and Raman mappings to prove the formation of interlocking interfacial polymer chains. Figure 2h shows a 3D porous network of two layers of hydrogels, and the average pore diameters of the SL and RL were $\sim 9.5 \mu\text{m}$ and $13.2 \mu\text{m}$, respectively. And the resulting scaffolds support cell spreading, migration, and proliferation²⁹. Moreover, the two layers completely combined with each other, and the transition layer could be observed at the interface without a distinct boundary, which strongly proves that the two-layer networks have penetrated into each other in the process of SEIP and converged into a whole. The interlocking structure and continuous features of the JHA were also confirmed from the Raman mapping image in Fig. 2i. This interlocked structure firmly bonded the two layers, and the RL could effectively transfer the strain to the SL through the interlocking structure, avoiding fracture and delamination, thereby achieving stable and robust adhesion to biological tissues. In addition, as shown in the atomic force microscopy (AFM) images (Fig. S5), after the RL was formed at the interface in situ, the surface roughness of the hydrogel increased from $19.9 \mu\text{m}$ to $28.4 \mu\text{m}$, which increased the contact area and friction between the hydrogel and biological tissues at the microscopic level to promote interfacial adhesion. Furthermore, the increase in surface roughness of the JHA combined with its loose extracellular-matrix-like pores could facilitate the adhesion of fibroblasts to hydrogels and promote wound repair^{30,31}.

Adhesive plugging performance of JHA in moist and dynamic environments

In SEIP process, the surface blood and water were self-confined as components within the in-situ formed RL hydrogel to counteract their detrimental effects on wet interface, while PAA and CS/CSMA in JHA formed physical interactions (for example, hydrogen bonds and electrostatic interactions) with tissue surface, resulting in instantaneous adhesion. Subsequently, the NHS ester groups grafted on AAC formed covalent bonds with the primary amine groups on the tissue, ensuring stable adhesion. To evaluate the adhesion performance of the JHA, we conducted two types of mechanical tests: the interfacial toughness was measured via 180° peel tests, and the shear strength was measured by lap-shear tests. Wet porcine skin is mechanically stable and similar to human skin, so it was selected as model tissue to evaluate the adhesion performance of JHA under different conditions.

First, the effect of the pressing time on the adhesion performance of the JHA hydrogel was explored. The adhesion strength increased with pressing time increasing within 30 min, implying that covalent cross-links gradually formed between the hydrogel and the surface of tissues (Fig. S6a, c). The hydrogel demonstrated tough and strong adhesion to wet porcine skins, achieving an interfacial toughness greater than 360 J m^{-2} and a shear strength exceeding 34 kPa, upon contact and application of gentle pressure (1 kPa) for less than 10 min (Fig. S6b, d). The ability to form stable covalent adhesion in a short time provides feasibility for its application in clinical surgery. When pressing time reached 30 min, the adhesion strength of the hydrogel to wet porcine skin reached the maximum and maintained a balanced state (with an interfacial toughness of 440 J m^{-2} and a shear strength of 80 kPa). In addition, the adhesion performance of the JHA hydrogel also greatly depended on the amount of RL precursor solution. When

the amount of RL precursor solution was $125 \mu\text{L cm}^{-2}$, the adhesion strength of the hydrogel peaked, with an interfacial toughness of 455 J m^{-2} (Fig. S7a, b) and a shear strength of 100 kPa (Fig. S7c, d). Too little or too much application of the RL precursor solution decreased the adhesion strength of the hydrogel. When the amount was too low, it was not conducive to forming an interlocking structure with the SL and covalently bonding with biological tissues. When the amount was too large, the formed repairing layer was too thick, which made it difficult to transfer the strain to the SL when subjected to external force, so that the phenomena of fracture and delamination occurred, and the hydrogel separated from the tissue surface. Furthermore, the JHA was covalently crosslinked with the amino groups on tissue surface through NHS ester groups to provide stable adhesion. Therefore, the number of NHS ester groups in the hydrogel network also influenced on adhesion (Fig. S8). When the AAC-NHS content in the system was less than 1.25% (w/w), the adhesion strength increased with increasing NHS ester group content, indicating that the number of covalent bonding sites increased. When the content increased to 1.25%, the adhesion strength reached the maximum and remained stable (the interfacial toughness was 524 J m^{-2} , and the shear strength was 105 kPa).

The hydrogel adhesive can be applied to various wet tissues, including the skin, muscle, small intestine, stomach, heart, and liver. Figure 3a–c shows the adhesion strength of the JHA to different biological tissues. The adhesion strength to the skin was the most robust, with an interfacial toughness up to 524 J m^{-2} , and the shear strength reached 105 kPa. The adhesion strength to the muscle, liver, intestine, heart, and stomach increased in turn, with interfacial toughness values of 289 J m^{-2} , 318 J m^{-2} , 326 J m^{-2} , 351 J m^{-2} , and 491 J m^{-2} and shear strengths of 20 kPa, 39 kPa, 44 kPa, 68 kPa, and 81 kPa, respectively. In addition, when the hydrogel adhesive was adhered to different biological tissues for 180° peeling tests (Fig. S9), peeling hysteresis was generally observed, which proved that the adhesion between the JHA and different biological tissues had great interfacial toughness. Compared with existing medical tissue adhesives, JHA exhibited superior adhesion properties (Fig. 3d, f). We found that most commercially available tissue adhesives exhibited limited adhesive strength for tissues with an interface toughness of less than 30 J m^{-2} and a shear strength of less than 15 kPa. Among existing tissue adhesives, although cyanoacrylate adhesives (such as Compant) have relatively good adhesion properties (with an interfacial toughness exceeding 230 J m^{-2} and a shear strength exceeding 70 kPa), this type of adhesive forms a rigid glassy layer after curing, which hardens the interface and restricts the movement of tissues^{32,33}.

Since the JHA was applied in a dynamic environment, 200 cyclic loading-unloading tensile tests (30% tensile strain) were carried out under adhered state to evaluate the adhesion ability of the hydrogel in dynamic environment. As shown in Fig. 3g, the maximum force value remained at almost the same level in each cycle, indicating that the JHA exhibited an excellent fatigue-resistant tissue adhesion ability in dynamic environment. During the cycling process, the JHA always tightly bonded with tissues and remained stable in the bulk by dissipating energy, which demonstrated that the hydrogel possessed not only excellent tissue adhesion ability but also bulk cohesion strength. Additionally, the interfacial toughness of the JHA before and after 200 cycles of loading-unloading tests is shown in Fig. 3h, and no significant decrease was observed. In conclusion, the JHA possesses stable and robust adhesion strength and can be used for plugging and repairing penetrating wounds in moist and dynamic environments.

To demonstrate the adhesive plugging ability of the JHA, we further evaluated its capacity as a liquid-tight sealing adhesive in New Zealand rabbit models with a $2 \text{ cm} \times 1.5 \text{ cm}$ POF (Fig. 3i). The precursor (i.e., the RL) was first injected onto the surface of the GOx-entrapped SL, and then placed on the fistula wound intraorally. After 1 min of gentle pressing, the hydrogel was fully attached to the defect. The

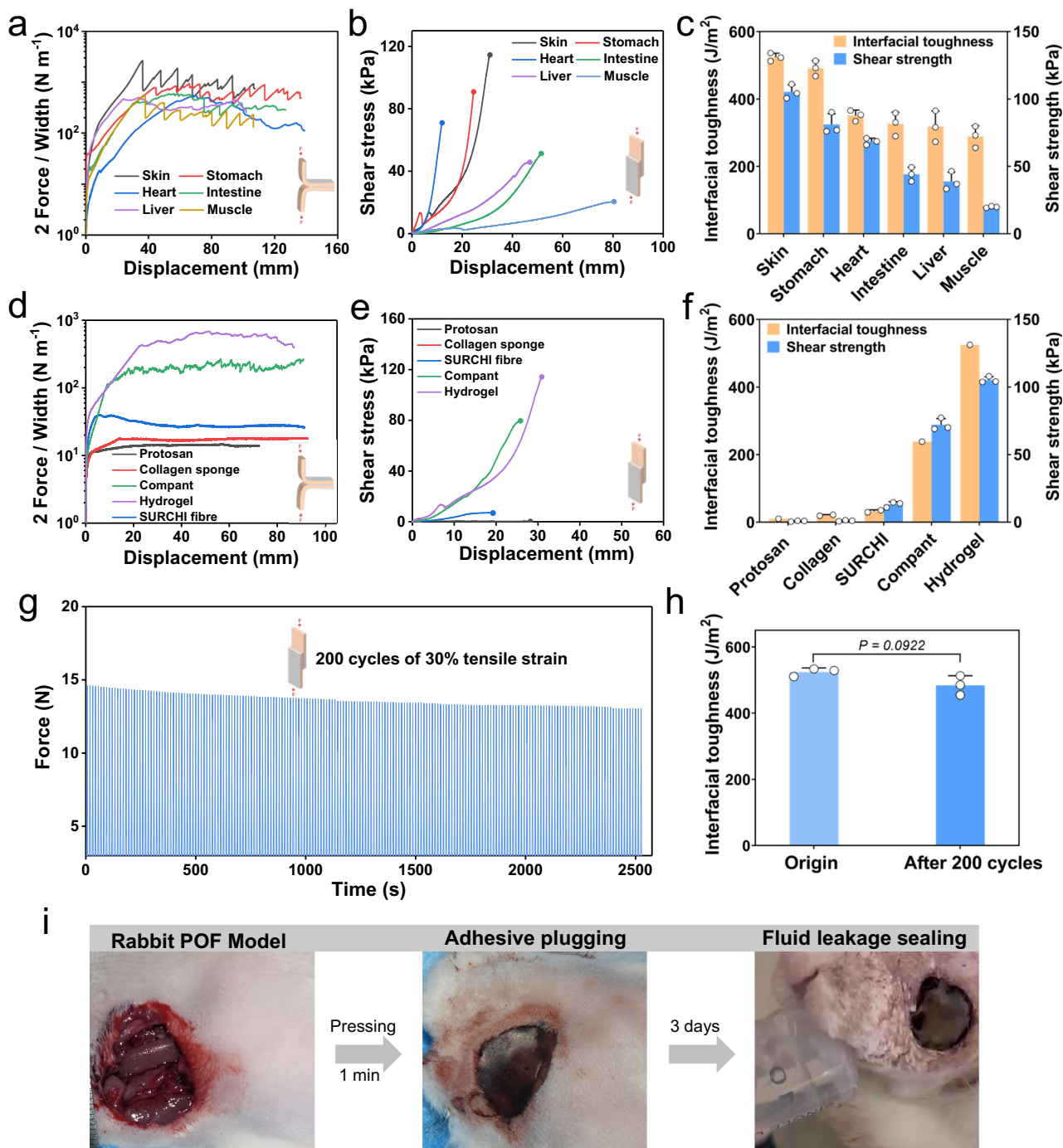


Fig. 3 | Adhesion performance of the JHA adhered to wet tissues. **a** Curves of 180° peeling tests for various tissues adhered by JHA. **b** Curves of lap-shear tests for various tissues adhered by JHA. **c** Interfacial toughness and shear strength between various tissues adhered by JHA. **d** Curves of 180° peeling tests for the JHA and various commercially available tissue adhesives adhered to porcine skin. **e** Curves of lap-shear tests for the JHA and various commercially available tissue adhesives adhered to porcine skin. **f** Comparison of adhesion performance between the JHA

and various commercially available tissue adhesives. **g** Cyclic loading-unloading curves of the JHA adhered between porcine skins. **h** Interfacial toughness of the JHA before and after 200 cycles of loading-unloading tests. **i** Adhesive plugging of the JHA in New Zealand rabbit POF models. Data are shown as mean \pm s.d. ($n = 3$ independent samples in **c**, **f**, **h**). Two-sided unpaired t-test was used for statistical analysis of (**h**).

adhered JHA maintained adhesion in the New Zealand rabbit POF model with a normal diet for more than 3 days without any sign of decreased adhesion. Then, we further attested its sealing functions using peroral saline injections in these POF models, which provides excellent fluid-tight sealing without water seeping or flowing out (Fig. 3j and Supplementary Movie 1). To further investigate the adhesive feasibility of the JHA in conditions lacking blood or glucose, we

performed it on rat models of full-thickness skin wound infection by supplementing the RL precursor with glucose (Fig. S10). It can be visually observed that the JHA hydrogel adhered firmly to the infected wound, forming a tight seal between the defect and the hydrogel, and this robust adhesion persisted for over 3 days without any signs of detachment. These data demonstrated the effective wound-sealing capacity of the JHA, even in environments devoid of blood or glucose.

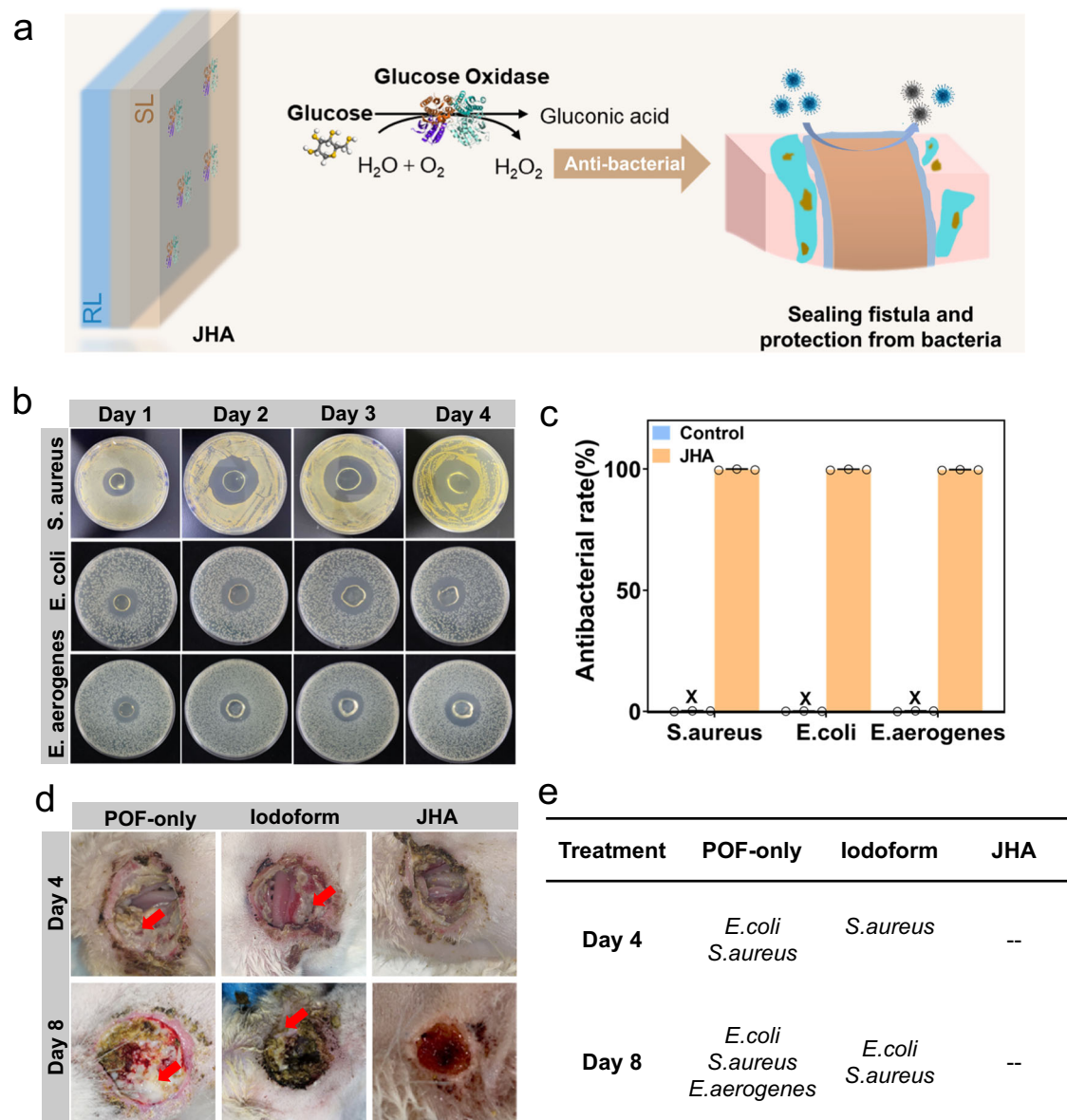


Fig. 4 | Antibacterial ability of the JHA. **a** Schematic diagram of the antibacterial effect of the JHA. **b** Images of inhibition zone on culture plates after *S. aureus*, *E. coli* and *E. aerogenes* co-cultured with JHA, respectively. **c** Bacteriostatic rate of the JHA

against *S. aureus*, *E. coli* and *E. aerogenes*, respectively. Data are shown as mean \pm s.d. ($n = 3$ independent samples). Images (**d**) and bacterial colonies (**e**) in the wounds of rabbit POF models for different groups on day 4 and 8.

In addition, the degradation behavior of the JHA was also investigated to assess its adhesion stability. As shown in Fig. S11, there was no significant disintegration behavior observed for JHA hydrogel during the 30 days immersion in artificial saliva, and it remained almost intact, indicating minimal degradation of the JHA, contributing to long-term stability for in vivo POFs sealing. These results suggest that the JHA could serve as an effective and stable sealant and adhesive to seamless plug POF wounds.

Antibacterial activity of JHA towards the external environment

The epidermis and mucosa provide a protective barrier from the external environment. POF wounds without protective barriers, combined with a prolonged warm, humid and food-contaminated oral environment, facilitate favorable conditions for the growth of various bacteria in the oral cavity. These factors lead to severe wound infection at the fistula, which can delay wound healing or even be life-threatening. Due to its superior sealing ability, the JHA can isolate

irritants and microorganisms in the oral cavity to prevent bacterial growth. Moreover, in the process of wound sealing, the SL-surface GOx can catalyze the conversion of O_2 and glucose in the blood to produce H_2O_2 in the interlocking layer of JHA. When the toxic H_2O_2 diffuses through the SL hydrogel towards the intra-oral side, it effectively destroys the bacterial protein molecular structure due to oxidation, thereby achieving sterilization on the wound surface. The schematic diagram is shown in Fig. 4a and Fig. S12. Meanwhile, if the toxic H_2O_2 diffuses through the RL hydrogel towards the inner mucosal side, it would be scavenged by the $Fe[Gly]_2$ that exhibits peroxidase-like activity confined in the RL hydrogel, protecting the cells from ROS-mediated oxidative damage, ensuring the biosafety of the JHA and unhindered wound healing.

As a proof-of-concept study, the antibacterial activity of the JHA was then comprehensively estimated in vitro and in vivo. Before the antibacterial test, the bacterial species of the POF wounds were firstly analyzed using New Zealand rabbit POF models, as presented in Fig. 4e.

Escherichia coli (*E. coli*), *Staphylococcus aureus* (*S. aureus*, gram-positive), and *Enterobacter aerogenes* (*E. aerogenes*, gram-negative) were detected as the three most abundant bacterial species in the POF group. Based on these results, we subsequently used *E. coli*, *S. aureus*, and *E. aerogenes* as model bacteria to conduct the in vitro antibacterial tests. The images of the inhibition zone shown in Fig. S13 revealed that there were no inhibition zones on the culture plates after cocultivation with GOx-free SL hydrogel, indicating that pure SL hydrogel has no antibacterial activity. In contrast, after cocultivation with JHA, obvious inhibition zones appeared on the culture plates, and the inhibition zones were still clearly visible on the 5th day (Fig. 4b), indicating that the GOx/Glu system endowed the hydrogel with sustained antimicrobial activity. Next, the turbidity of bacterial liquid was characterized (Table S2), thereby quantitatively calculating the antibacterial rate of the hydrogel. As expected, the antibacterial rates of the JHA against the three different bacterial species were all >99% (Fig. 4c), indicating the excellent antibacterial ability of the JHA.

In the following animal model experiments, we further examined the bacterial inhibition of the JHA using New Zealand rabbit POF models. The POF-only group and Iodoform group (commonly used in surgery) were used as controls. The bacterial colonies at the wound sites were swabbed for evaluation at different observation time points, and the results were displayed in Fig. 4e. It can be seen that *S. aureus*, *E. coli* and *E. aerogenes* were detected in the wounds of POF-only group, and *S. aureus* and *E. coli* were also found in the Iodoform group, while no harmful strains were detected in the JHA group, indicating the excellent antibacterial effect of the JHA. Meanwhile, the typical images of the POF wounds with three different treatments at 4 days and 8 days were also captured. As shown in Fig. 4d, both the POF-only and Iodoform groups showed purulent conditions, as highlighted by the red arrows in the images, which often indicates an ongoing bacterial infection or inflammation. In contrast, there was no apparent purulent condition observed in the JHA group. Combining the results of the antimicrobial tests, we suggest that the JHA may reduce purulent necrosis in tissues with the help of its antibacterial effects, which is highly beneficial for wound healing.

Furthermore, we have conducted the 16s analysis to investigate the bacterial diversity in POF wounds. The species abundance and diversity analysis of the POF wound microbiota were first investigated. As shown in Fig. S14a, the JHA group exhibited a significant reduction in species numbers. Furthermore, a heatmap in Fig. S14b also showed the noticeable differences in the type and amount of gene expression between JHA and POF-only groups. Then, the changes in microbial abundance of the POF wound were analyzed, and the relative abundance of the microbiota varied at the genus levels between the POF-only and JHA groups, as shown in Fig. S14c, d. Compared with the POF-only group, the proportion of pathogenic bacteria such as *Rodentibacter* and *Escherichia-Shigella* in JHA group was effectively reduced, while the proportion of normal bacteria was significantly increased. These normal bacteria could be beneficial for the health of oral microenvironment by competitively inhibiting harmful microorganisms and modulating oral immune responses, which contributes to enhanced wound healing.

In vitro biocompatibility, antioxidant and immune regulation property

To evaluate the biocompatibility of the hydrogels, first, we evaluated the cytotoxicity of the SL powders, extracted solutions of the RL hydrogel, SL powders and JHA powders and performed an in vitro cytotoxicity assay via the Cell Counting Kit 8 (CCK-8) assay. A mouse fibroblast line (L929) was selected as a cell model for coculture with the RL precursor, SL powders and JHA powders. After coculture for 24 h and 48 h, the cell viability exceeded 90%, demonstrating the excellent biocompatibility of the hydrogels (Fig. S15a–c). Moreover,

increasing the hydrogel concentration tended to promote cell proliferation, which may be attributed to the presence of CS and CSMA. Second, LIVE/DEAD staining of L929 cells cocultured with an extracted solution of RL, SL powders or JHA powders incubated in media for 24 h revealed cell viability comparable to that of the control media group (Fig. S15d). Only individual dead cells were detected, and live cells still maintained a normal morphology, which confirmed the excellent cytocompatibility of our JHA.

The oxidative microenvironment and inflammation at the wound site can produce reactive oxygen species (ROS), thereby hindering the healing of wound tissues. Integrating antioxidants into hydrogel adhesives can effectively scavenge ROS and improve metabolic processes, which is highly important for wound healing. The Fe[Gly]₂ in the catalytic system not only catalyzes polymerization but also endows the hydrogel with a significant antioxidant effect in the process of wound treatment and protects cells from ROS-mediated oxidative damage due to its peroxidase-like activity, as mentioned above. In this study, the in vitro antioxidant capacity of the RL hydrogel was investigated via the DPPH free radical scavenging test and the ROS scavenging test. The free radical scavenging rate was dependent on the Fe[Gly]₂ concentration (Fig. 5a–c and Fig. S16a–c). The hydrogel exhibited the highest scavenging rate of DPPH free radicals (reaching 75.3–94.8%), and the scavenging rates of $\cdot\text{OH}$ and H_2O_2 were 56.8–78.5% and 66.4–93.2%, respectively. In addition, the hydrogel exhibited the highest scavenging efficiency for DPPH free radicals in a shorter time, while it took a longer time to scavenge H_2O_2 (Fig. 5a–c and Fig. S16d), possibly because the system was initiated by H_2O_2 generated from GOx/Glu, and the production and consumption of H_2O_2 maintained a relatively balanced state in the initial stage of the reaction. Moreover, the cytoprotective ability of JHA was explored by incubating L929 cells with RL hydrogels under oxidative stress (100 μM H_2O_2). We examined the variations in intracellular ROS levels through the ROS indicator DCFH-DA. As shown in Fig. 5d, compared with that of the H_2O_2 control group, the green fluorescence intensity of the cells cocultured with the RL hydrogel decreased significantly and weakened with increasing Fe[Gly]₂ content, indicating that the Fe[Gly]₂ in JHA can effectively attenuate intracellular oxidative stress, which provides a favorable biochemical microenvironment for cell proliferation and differentiation.

Furthermore, the anti-inflammatory and immunomodulatory effects of RL hydrogels were assessed on murine RAW264.7 macrophages in the presence of lipopolysaccharide (LPS). Immunofluorescent staining was first performed to identify M1 and M2 macrophages after 48 h of co-culture with RL hydrogels, using inducible nitric oxide synthase (iNOS) and CD206 to mark the M1 and M2 phenotypes, respectively. As presented in Fig. 5e, the RL hydrogel group exhibited a lower number of iNOS-labeled M1 macrophages and a higher number of CD206-labeled M2 macrophages compared to the LPS-treated group. Additionally, the immunofluorescent staining results also revealed that the RL hydrogel could significantly decrease the release of inflammatory cytokines (IL-6, TNF- α , and IL-17) from macrophages (Fig. 5f, g and Fig. S17). To further assess the macrophage phenotype on the RL hydrogels, the mRNA expression levels of pro-inflammatory markers (iNOS, IL-6, TNF- α) and anti-inflammatory marker (CD206) were quantified using PCR. As shown in Figs. 5h and i, the expression levels of iNOS, IL-6, and TNF- α in macrophages co-cultured with RL hydrogels were markedly reduced, whereas the expression of CD206 was elevated. These results confirmed that the hydrogels mitigated the inflammatory response and effectively polarized macrophages towards an anti-inflammatory phenotype. This effect can be attributed to the exceptional antioxidant activity of JHA, which efficiently reduced ROS levels, alleviated oxidative stress, and subsequently modulated the immune microenvironment.

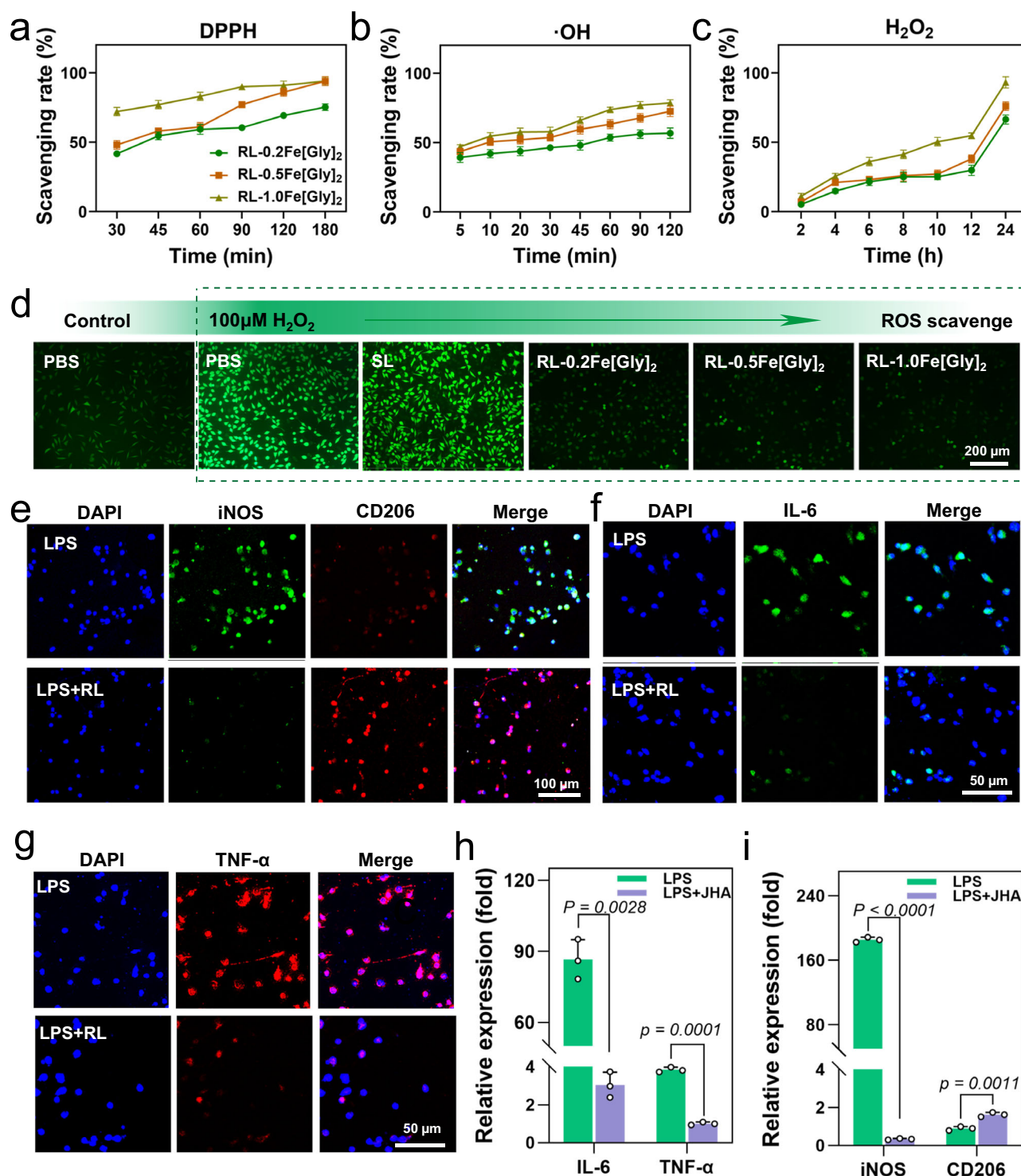


Fig. 5 | Antioxidative and anti-inflammatory ability of hydrogel. Scavenging rates of the RL hydrogels for DPPH (a), ·OH (b), and H₂O₂ (c) after co-incubation for different times. **d** Alleviation of oxidative stress in L929 cells using DCFH-DA as ROS indicator after different treatments. **e–g** Immunofluorescence staining of iNOS, CD206, IL-6 and TNF- α in RAW 264.7 cells after treatment with RL hydrogels

in the presence of LPS, and cell nuclei were stained with DAPI (blue). **h, i** The relative mRNA expression levels of iNOS, CD206 and IL-6, TNF- α in RAW 264.7 cells treated with RL hydrogels. Data are shown as mean \pm s.d. ($n = 3$ independent samples in **a–c**, **h, i**). Two-sided unpaired t-test was used for statistical analysis of (**h, i**).

In vivo fistula healing performance of the JHA in the rabbit POF model

After demonstrating that the JHA exhibited excellent multifunctional properties for POF treatment, we next established New Zealand rabbit models of POF defects to evaluate the in vivo repair capacity of the as-prepared JHA. Similar to injuries due to facial traumas or post-

oncologic resections, a 2 cm \times 1.5 cm, oval and through-and-through wound penetrating both skin and oral mucosa was made on the anterior buccal region of each rabbit, and subsequently treated with JHA, Iodoform dressing and untreated (POF-only group), respectively. As illustrated in Fig. 6a, in JHA group, the RL precursor was first dropped on SL/GOx hydrogel with the size matching to the oral wound

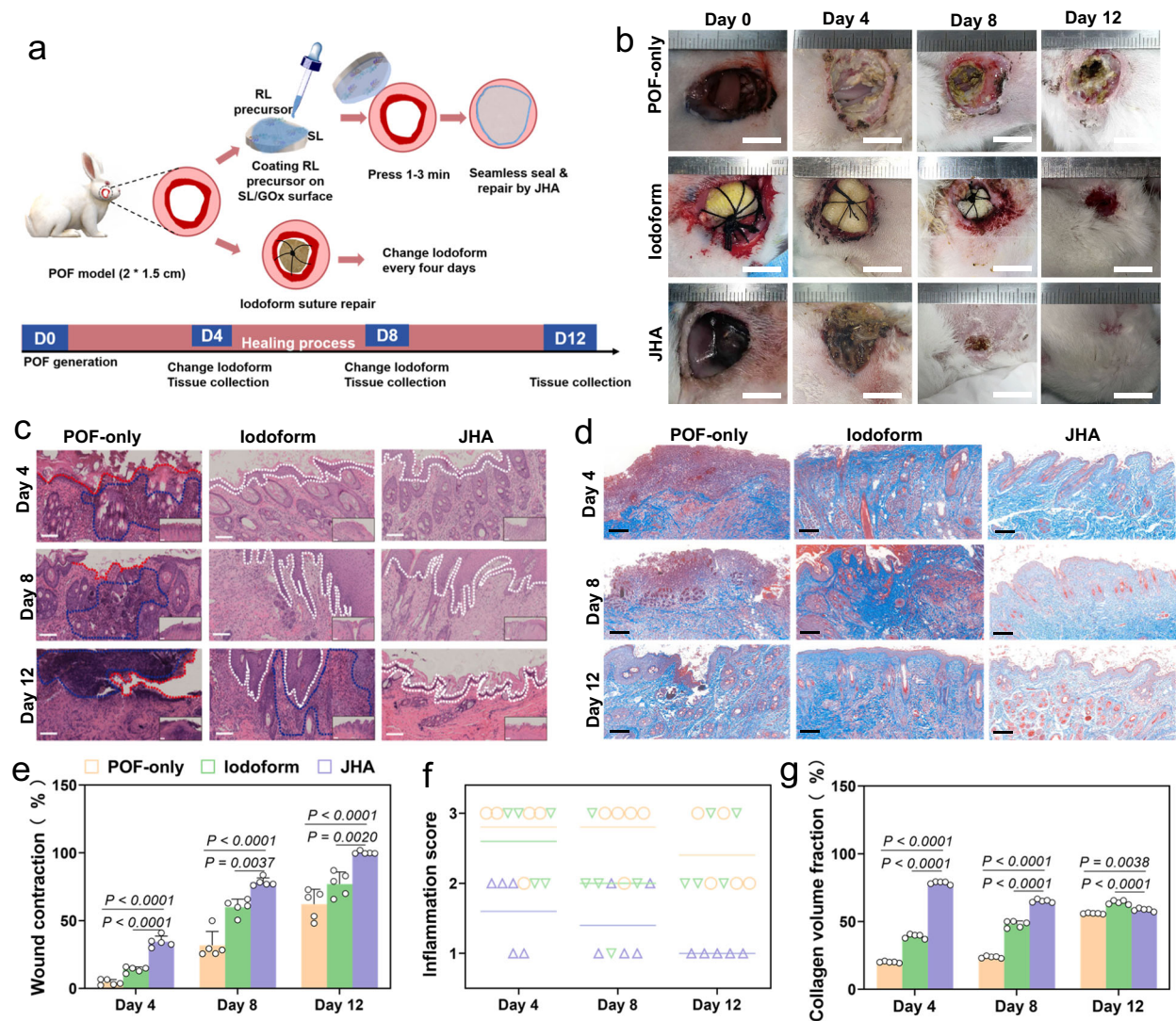


Fig. 6 | Analysis of the healing results of New Zealand rabbit POF models.

a Schematic diagram of the process of applying JHA to New Zealand rabbit POF model. **b** Representative photographs of wounds with different treatments from day 0 to day 12. Scale bar: 1 cm. **c** Optical microscopy images of skin side tissue regeneration in POF defects stained with H&E. The dashed box areas are magnified and shown below (White dashed line: intact epithelial layer; red dashed line: defective epithelial layer; blue dashed line: inflammatory area). scale bars in both

magnified images and insets: 300 μm. **d** Masson's trichrome staining of the skin side. Scale bar: 300 μm. **e** Wound healing rate at different times. **f** Graded assessment of inflammation degree in each group. **g** Quantification results of collagen volume fractions of the skin side. Data are shown as mean ± s.d. (n = 5 New Zealand rabbits in **e–g**). One-way ANOVA followed by Tukey's multiple comparison test was used for statistical analysis of (**e**, **g**).

and then placed on the intraoral wound bed, covering all the region of the wound. After 1 min of gentle pressing, the JHA was fully attached to the surface of the wound defect without further steps. In contrast, Iodoform required suture fixation, which took longer to perform (>5 min) and caused puncture-driven tissue damage. Besides, Iodoform dressing were changed every 4 days in the evaluation. Iodoform was folded into Vaseline gauze for wound packing to minimize tissue damage and prevent sticking.

To confirm the presence of JHA intra-orally, typical CLSM images were captured for POF wounds in New Zealand rabbits after JHA treatment, using SL labeled with FITC and RL labeled with Cy5.5. As presented in Fig. S18, the RL (red fluorescent) can be seen anchoring on the oral mucosal side of the POF wound, passing through the fistula, and coming into contact with the air, while the SL (green fluorescent) was positioned on the intraoral side, indicating that intraoral presence of the JHA. Then, representative pictures and the healing rate of the skin side wounds in different groups at scheduled time intervals were shown in Figs. 6b and 5e. The wounds both in JHA and Iodoform

groups exhibited significantly faster wound closure during the ongoing wound-healing experiment at different times (days 4, 8, and 12). Specifically, the JHA group and Iodoform group led to 78.4% and 60.2% wound closure on day 8, respectively, which were noticeably higher than that of the POF-only group (31.8%). Consistent with the healing effect of external skin wounds, the wound-healing changes in mucosal side are shown in the Fig. S19, the oral mucosal wounds both in POF-only and Iodoform groups failed to achieve complete closure, whereas JHA treatment significantly accelerated mucosal closure during the wound-healing periods, and it even achieved full healing by day 12. To further evaluate the repair ability of JHA, the mechanical strengths of the healed tissues were measured by tensile and compressive tests on the 12th postoperative day and then compared to those of normal tissues at the same site. The results showed that the tensile and compressive moduli of the healed tissues were not significantly different from those of normal tissues (Fig. S20a). For such through-and-through traumatic injuries, the RL hydrogel adhering to mucosal wound surface provided a healing interface to support cell migration

and proliferation, thereby directly speeding the regeneration and healing of the inter-oral mucosa. Following mucosal healing, the local microenvironment underwent further remodeling to accommodate skin cell growth, directing their migration toward the healing site, and subsequently accelerating the healing of the external skin. Thus, the JHA hydrogel played an active and beneficial role in facilitating the whole fistula healing during POF treatment, even though it did not come into direct contact with the extraoral skin surface.

The incomplete closure in POF wound may lead to potential infections, hinder normal diet, and affect nutrient absorption. As shown in Fig. S20b, the weight of the POF-only and Iodoform group decreased to 86.2% and 91.2% on day 4, respectively, and did not improve in the following treatment days. In contrast, all rabbits in the JHA group displayed normal feeding behavior with associated weight gain. We next conducted blood analyses, including complete blood counts (CBCs) and comprehensive serum biochemistry panels, to assess potential nutritional statuses and inflammatory reactions (Fig. S20c–g). In addition, a low level of red blood cells and hemoglobin, along with a high number of white blood cells and neutrophil granulocytes, were observed, suggesting severe malnutrition and inflammation in the POF-only group. The Iodoform group also showed a high number of white blood cells at day 4, while no abnormal health signals were detected in the JHA group during the healing period of 12 days. All these results macroscopically attest that JHA treatment provides relatively uncompromised food intake and stable nutrition levels, effectively inhibits bacteria and controls the level of inflammation to promote wound healing.

Microscopically speaking, the therapeutic efficacies and extents of tissue regeneration between JHA and other treatment modalities were compared via the haematoxylin and eosin (H&E) staining and Masson's trichrome staining of both the buccal cutaneous wounds and mucosal counterparts. As shown in Fig. 6c and Fig. S21a, more inflammatory cells infiltrated the wound tissues in POF-only and Iodoform groups than JHA group on day 4. While apparent continuous epidermal tissues of the skin and mucosa were observed in the JHA and Iodoform groups on days 8 and 12, revealing that these regions healed well. Furthermore, the degrees of epithelialization and the epithelial integrity of mucosa of JHA group were higher than those of Iodoform group. In contrast, the POF-only group showed undesirable healing with massive epithelial necroses during the whole observation periods (Fig. 6f). This was due to the antioxidant performance and seamless adhesion of the JHA, which is conducive to wound healing.

Proper collagen deposition and remodeling are important to improve tissue healing. Collagen is an important component in all phases of wound healing and impart integrity and strength to all tissues. Therefore, Masson's trichrome staining was used to visualize collagen in the buccal cutaneous and mucosal wounds (Fig. 6d, g and Fig. S21b, c). On day 4 and day 8, the collagen arrangement in POF-only and Iodoform group was less and heterogeneous, while higher, denser and more uniform collagen deposition was observed in the JHA, making the JHA group exhibit greater wound edge contractility, which accelerated the wound repair process. This intuitively shows the reason for the fastest wound repair in the JHA group. On day 12, collagen deposition in the JHA group no longer increased and showed a decreasing trend which prevent excessive inflammation for reducing scarring, while the POF-only group and Iodoform group showed continuous increase, indicating that inflammation delayed the healing time, stimulated scar formation, and slowed down the wound repair process. These results provide additional microscopic evidence that the JHA promotes the regeneration process and reduces scarring.

To comprehensively understand the mechanisms by which JHA reduces inflammation and promotes tissue repair, we further performed histological analysis of the wound sites, and the key biomarkers including interleukin-6 (IL-6), cell adhesion molecule-1 (CD31), alpha-smooth muscle actin (α -SMA), vascular endothelial growth

factor (VEGF), proliferating cell nuclear antigen (PCNA), 4-hydroxynonenal (4-HNE), 8-hydroxy-2'-deoxyguanosine (8-OHdG), iNOS, and CD206 were tracked using immunofluorescence staining to assess angiogenesis, cell proliferation, oxidative stress, and inflammatory levels, respectively. IL-6 is usually generated as a response to inflammation or tissue injury; therefore, immunostaining for activated IL-6 was first performed. In comparison with the POF-only and Iodoform groups, IL-6 expression after 4 days of treatment was substantially decreased in the JHA group (Fig. 7a, c), suggesting that the JHA effectively mitigates inflammatory responses. Re-epithelization and angiogenesis are crucial processes in wound repairing. Thus, we then stain α -SMA (α -smooth muscle actin and mature blood vessels), CD31 (endothelial cell marker for new blood vessels), VEGF (vascular endothelial growth factor) and PCNA (proliferation marker) for further analysis. The wound sections from the JHA group had more expression of α -SMA, CD31, VEGF and PCNA compared to the POF-only and Iodoform groups on day 4 (Fig. 7b, d, e and Fig. S22), indicating that JHA has good ability to promote angiogenesis, fibroblast aggregation, thereby facilitating wound healing.

Moreover, we also studied the antioxidant and anti-inflammatory capabilities of JHA by detecting the level of oxidative stress in wound tissues and the polarization of macrophages. As shown in Fig. 7f, h, significantly lower levels of 8-OHdG and 4-HNE were observed in the JHA-treated wounds compared to the POF-only and Iodoform groups on day 4, indicating that JHA could effectively relieve oxidative stress during the early stages of POF wound healing. Furthermore, a larger number of iNOS-positive M1 macrophages (green fluorescence) and lower levels of CD206-positive M2 macrophages (red fluorescence) were observed in the POF-only and Iodoform groups, in sharp contrast to the JHA-treated group, which exhibited fewer iNOS-positive M1 macrophages and more CD206-positive M2 macrophages (Fig. 7g, i), confirming that JHA not only suppressed the inflammation but also promoted the macrophage polarization. Together, the *in vivo* results strongly suggest that the JHA can significantly inhibit excessive oxidative stress and inflammation, promote rapid angiogenesis and cell proliferation, and facilitate wound healing.

In addition, due to the minimal degradation of JHA, it eventually detached from the POF site in the process of wound treatment, subsequently either being expelled from oral cavity or ingested along with food into the digestive system, and ultimately excreted from the body. Hence, the *in vivo* safety of the JHA was further assessed under conditions of POF treatment and ingestion, including routine blood analysis and tests for liver and kidney function. As shown in Fig. S23, there were no signs of acute toxicity related to either POF treatment application or digestion of JHA, demonstrating its excellent biosafety, even if ingested into the body.

In vivo fistula healing performance of the JHA in Beagle POF model

Encouraged by the successful and rapid wound healing results in the rabbit POF model, the effectiveness of the JHA in a preclinical setting was also explored in a model that can potentially be translated to human wounds. Thus, we further established a Beagle model with POF defects as a proof of concept to evaluate the wound healing effect of the JHA *in vivo*. Beagle dogs with similar ages and weights were randomly assigned into three groups (POF-only group, Iodoform group, and JHA group) with a 3 cm \times 2.5 cm oval buccal penetrating wound in each animal (Fig. 8a). Consistent with the data from rabbit POF models, the JHA treatment again proved to have a superior efficiency of wound healing and enhanced growth after such through-and-through facial trauma (Fig. 8b). The wound area reductions were mostly evident from observation day 4 to day 12 in the JHA group (Fig. 8c). Granulation healing was facilitated and eventually realized at day 22 in the JHA group. The tensile and compressive moduli of the healed tissues were still not significantly different from those of normal tissues (Fig. S24a),

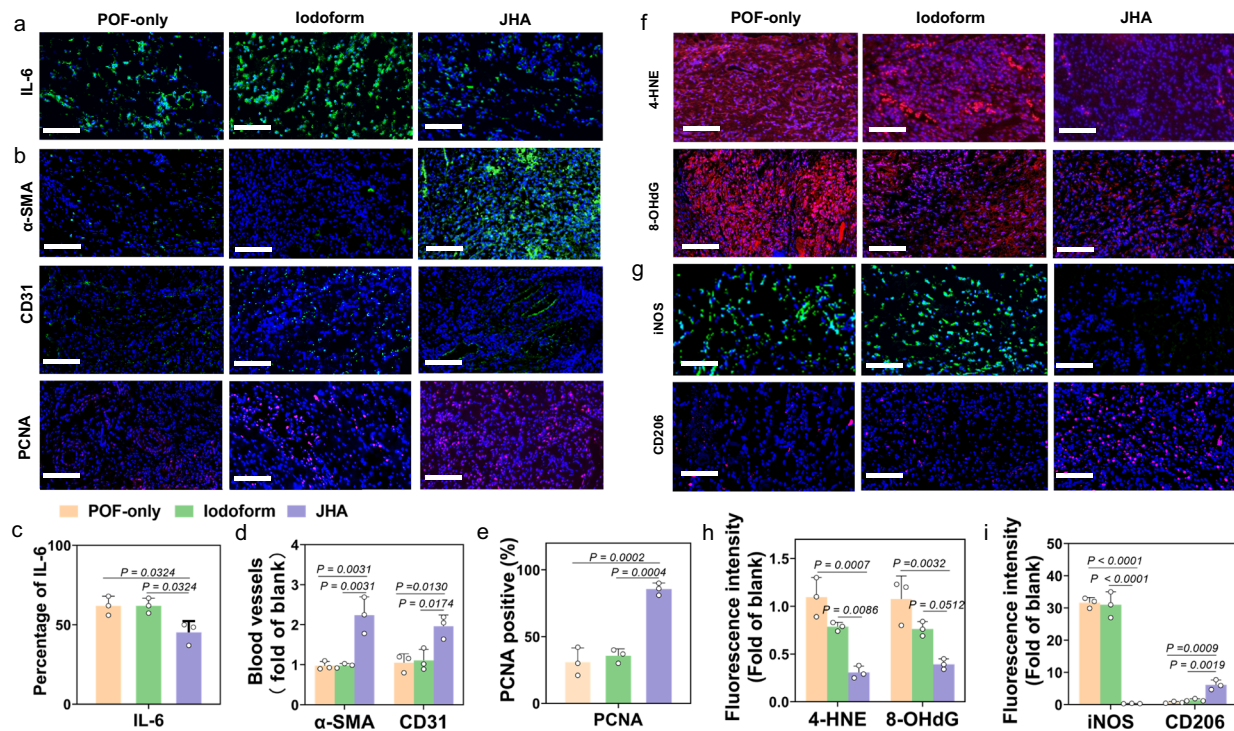


Fig. 7 | Immunofluorescence staining analysis of the POF wounds in different groups. a, b Representative immunofluorescence images for IL-6, α -SMA, CD31 and PCNA staining in different groups. Green, IL-6 or α -SMA or CD31; red, PCNA; blue, DAPI. Scale bar: 100 μ m. **c–e** Quantitative analysis of IL-6, α -SMA, CD31 and PCNA fluorescence intensity in different groups. **f** Representative immunofluorescence images for 4-HNE and 8-OHdG staining in different groups. Red, 4-HNE or 8-OHdG; blue, DAPI. Scale bar: 100 μ m. **g** Representative immunofluorescence images of

iNOS and CD206 in different groups. Green, iNOS; red, CD206; blue, DAPI. Scale bar: 100 μ m. **h** Quantitative analysis of 4-HNE and 8-OHdG positive regions in different groups. **i** Quantitative analysis of iNOS and CD206 positive regions in different groups. Data are shown as mean \pm s.d. ($n = 3$ New Zealand rabbits in **c–e, h, i**). One-way ANOVA followed by Tukey's multiple comparison test was used for statistical analysis of (**c–e, h, i**).

while the other two groups revealed persistent through-and-through wounds, resulting in fistula formations in both groups on day 22. To further investigate the efficacy and degree of tissue regeneration of JHA and other treatment methods, a comparison was made between H&E staining and Masson's trichrome staining on the buccal cutaneous wounds and mucosal wounds. As shown in Fig. 8d, more inflammatory cells infiltrated the wound tissues in the POF-only and Iodoform groups than that in JHA group. Undisturbed by saliva and chewing due to its physicochemical characteristics, the JHA hydrogel largely and indirectly provided a beneficial environment for re-epithelialization. Larger bundles of collagen deposits were also found in the JHA-treated groups (Fig. 8e, f) when compared to those of the other two groups in Masson's trichrome staining, which was consistent with the macroscopic wound healing trends.

For further assessment of the rehabilitation of wound healing, IL-6, α -SMA, CD31 and VEGF were traced by immunofluorescence analyses to evaluate the inflammatory, myofibroblast, and angiogenesis process, respectively (Fig. 8g, h). Compared with POF-only and Iodoform groups, IL-6 expression was substantially decreased in the JHA group on day 22, such results were also confirmed by H&E staining. In addition, more α -SMA, CD31 and VEGF positive cells were observed in the JHA group. This finding was likely due to the fact that JHA-directed healing was achieved by the inhibition of undesirable local inflammation (saliva and food), while at the same time, JHA treatment, via advantageous environmental barriers, enhanced this process via rapid angiogenesis and the promotion of both epithelial and fibrotic cells.

Importantly, JHA was devoid of any notable toxicity during the treatment period (22 days). The biosafety evaluation showed no changes in key blood biochemical markers, including alanine transaminase (ALT), aspartate transaminase, urea, creatinine, triacylglycerol, and total cholesterol (Fig. S24b), suggesting that liver and kidney

functions were unaffected, demonstrating good biocompatibility after JHA dressing. In addition, The H&E staining results also showed no apparent pathological changes in the major organs of the treated beagles (Fig. S24c), indicating that JHA not only effectively promote POF wound healing, but also have good biosafety. These results firmly support the conclusion that the JHA could provide leak-free sutureless plugging and favorable biochemical environment to facilitate tissue repair and shorten wound healing time, indicating its promising clinical application for leak-related tissue sealing and healing.

RNA sequencing and analysis

To identify the potential signaling pathways involved in the rapid healing of the oral through-and-through defects in the JHA group, RNA sequencing (RNA-Seq) analyses were utilized to compare the messenger RNA (mRNA) differences among the POF-only and JHA groups in two different observation time zones using New Zealand rabbit POFs as models. Compared with the POF-only group, JHA groups have 450 and 166 differentially expressed genes on day 4 and day 12, respectively. According to the results obtained from the heat maps of different gene expressions in the immune (inflammatory) system, all the major significant discrepancies are revealed on various observation time zones (Fig. 9a and Fig. S25a). Differential genes enriched in signal transduction of such system were recognized. As a further attempt to decipher the most likely pathways relevant to the immune (inflammatory) system, the top 20 KEGG enrichment genes (pathways) were analyzed after RNA-seq between the POF-only and the JHA groups (Fig. 9b and Fig. S25b). Our results revealed that different expressed genes in these new regenerated tissues ($p \leq 0.1$) are mainly enriched in cytokine-cytokine receptor interactions, Janus kinases/signal transducer and activator of transcription proteins (JAK/STAT) pathway, Th-17 signaling pathway and IL-17 signaling pathway, bespeaking of the

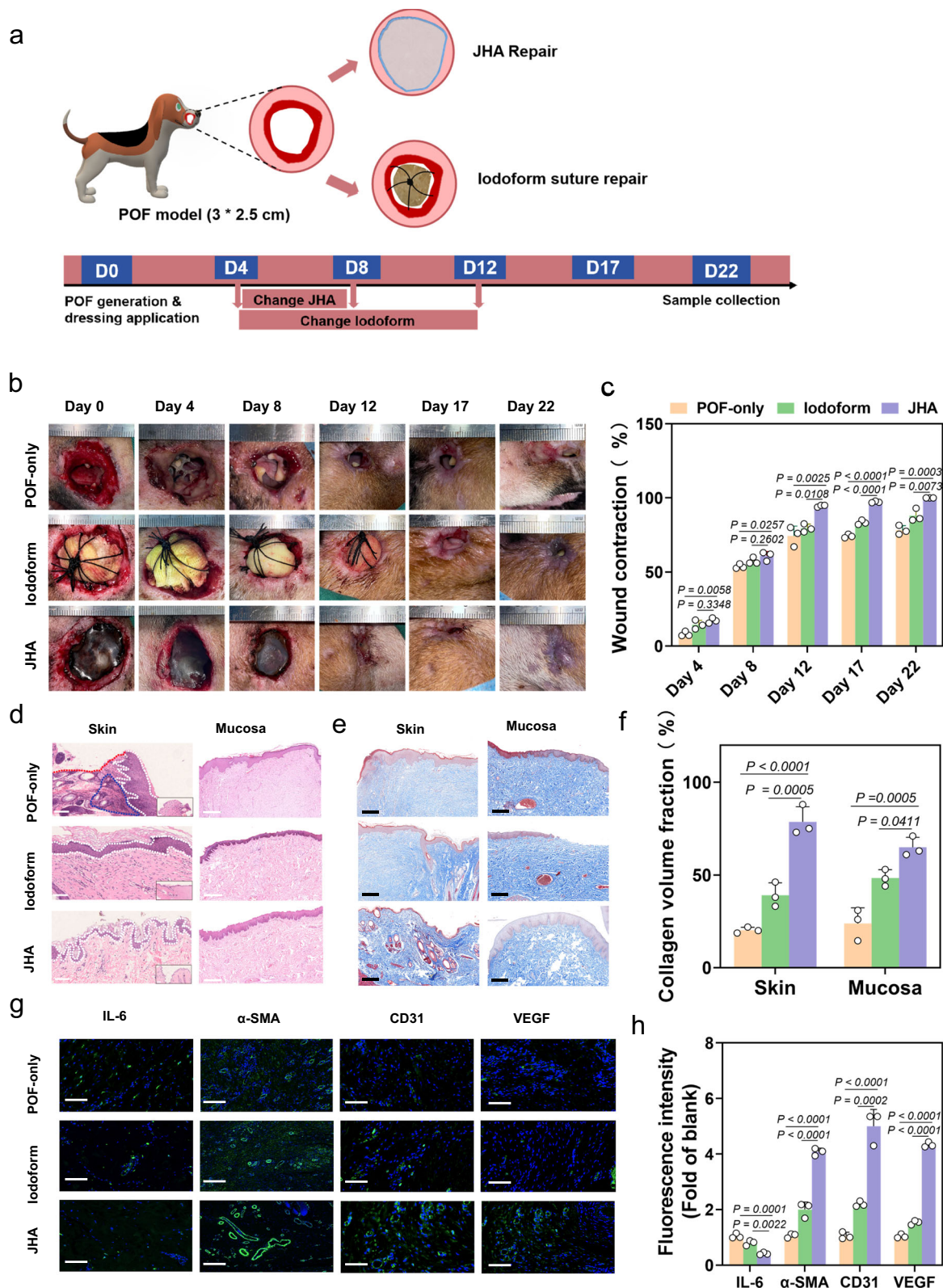


Fig. 8 | Analysis of the healing results of the Beagle POF models. **a** Schematic illustrating the POF defect and treatment schedule in the Beagle model. **b** Representative photographs of wounds with different treatments from day 0 to day 22. **c** Wound healing rate at different time. **d** H&E staining of the skin side and mucosal side after 22 days of treatment. The dashed box areas are magnified and shown below (White dashed line: intact epithelial layer; red dashed line: defective epithelial layer; blue dashed line: inflammatory area). scale bars in both magnified

images and insets: 400 μ m. **e** Masson's trichrome staining and **(f)** corresponding quantification results of collagen volume fractions of the skin side and mucosal side after 22 days of treatment. Scale bar: 200 μ m. **g** IL-6, α -SMA, CD31 and VEGF immunofluorescence staining images and **(h)** quantification analysis of wounds treated for 22 days. Scale bar: 100 μ m. Data are shown as mean \pm s.d. (n = 3 Beagle dogs in **c, f, h**). One-way ANOVA followed by Tukey's multiple comparison test was used for statistical analysis of **(c, f, h)**.

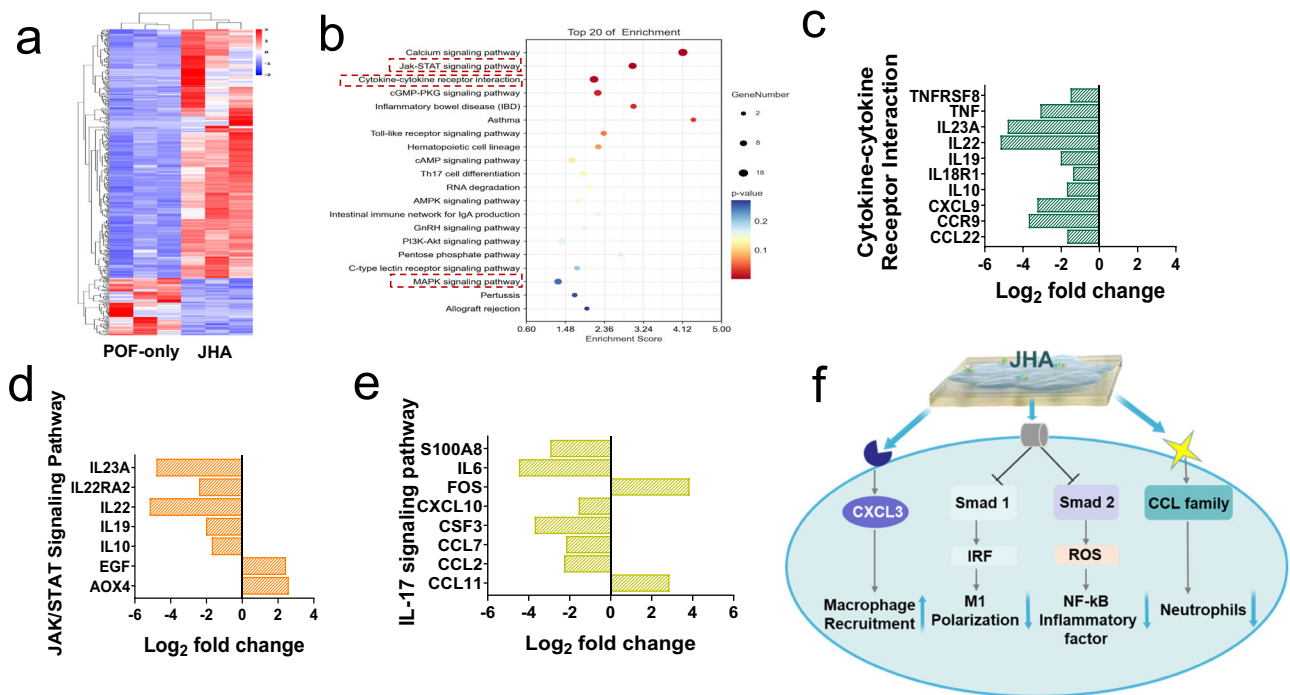


Fig. 9 | Sequencing analysis of the process of New Zealand rabbit POF repairing by JHA treatment. **a** Heat maps of regenerated tissues between POF-only and JHA groups on day 4. **b** Top 20 genes in KEGG enrichment analysis of treated samples after mRNA sequencing between POF-only and JHA groups on day 4, including representative top 20 upregulated or downregulated pathways. **c–e** Fold change of

gene expressing in cytokine-cytokine receptor interaction, JAK/STAT signaling pathway and IL-17 signaling pathway between POF-only and JHA groups on day 4. **f** Schematic of the JHA promoted POF healing by recruited macrophages, reduced neutrophils over enrichment, inhibited M1 macrophage polarization and suppressed ROS production.

cytokine-driven or macrophage-induced host immune defense contributing to final healing/unhealing outcomes. Chemokine networks are known for coordinating inflammatory responses through cell surface receptors of the seven-transmembrane domain of G protein-coupled receptor family³⁴. According to our results, within the (C-C motif) ligand (CCL) family, the pro-inflammatory CCL2, CCL7, CCL11, and CCL22 were also found downregulated in Day 4 and Day 12 observation point when comparing the JHA group with the POF-only counterpart, indicative of less recruitment of neutrophils (Fig. 9c–e and Fig. S25c–e).

Besides, the downregulation of IL-6 and IL-10 in the JHA groups also shed light on the intercellular signaling changes causing inflammation amelioration. The term, JAK-STAT, refers to molecules mediating the intracellular inflammatory signaling pathway, which can be activated by numerous chemokines, interferons, IL-6 or IL-10^{35,36}. The JAK/STAT undergoes dimerization after binding the aforementioned extracellular activators. Such change will induce the phosphorylation of both JAK and STAT, which eventually lead to canonical translocation and activation of nucleus gene transcription, causing enhanced inflammation^{37,38}. On the other hand, C-C chemokine receptor (CCR) 9, a special chemokine with combination of CCL25, has been found to colocalize with CD14+ and CD68+ macrophages (M1 macrophage) and are abundant in rheumatoid arthritis synovium and inflammatory bowel disease colitis^{39,40}. Aside from such macrophage polarization, the expression of CCR9/CCL25 dimers can also stimulated the production of IL-6, matrix metalloproteinases (MMP)-3 and tumor necrosis factor (TNF)- α in the surround microenvironment or peripheral blood samples⁴¹. In addition, it has been reported that T helper type 17 (Th17) cells may trigger exaggerated inflammatory responses when affected^{42,43}. IL-17, a pleiotropic pro-inflammatory cytokine is generated by Th17 cell, can exert its proinflammatory effects through IL-6, IL-8, TNF- α and granulocyte-macrophage colony-stimulating factor (CSF)^{44–46}. These molecules may facilitate the recruitment, activation

and migration of neutrophils to wound tissues, contributing to skin or mucosal injury. Furthermore, IL-17 can work synergistically with TNF- α to activate the NF- κ B, ERK1/2, and p38 signaling pathways, leading to IL-17C secretion from the surrounding tissues, which may amplify the inflammatory immune response^{43,44}. IL-17A may also enhance fibroblast proliferation through metabolic reprogramming, and connect the established profibrotic molecules such as TGF- β , and novel profibrotic mediators TL1A/DR3 and Ang-II⁴⁴. In our study, IL-17 excretion and its downstream effectors' levels are downregulated by the application of gel in the oral fistula when compared with the control group, revealing decreased inflammation and fibrosis in the target wound areas. Taken together, it is now assumed that both the cytokine/JAK/STAT and Th-17/IL-17 pathways are hinted or partially responsible for the rapid healing of oral fistulas via fibrosis, inflammation inhibitions and immunoregulation in the JHA group in vivo (Fig. 9f).

Discussion

Penetrating orocutaneous or oropharyngeal fistulas (POFs), featuring a highly moist environment, continuous saliva output, contamination from food intake, and repeated mechanical stimuli, remain a complicated and intractable clinical challenge for effective treatment, highlighting the critical importance of developing effective therapeutic strategies and solutions. To address these concerns, we herein propose a Janus hydrogel adhesive (JHA) constructed by wound surface enzyme-initiated polymerization (SEIP) method for POFs sealing and accelerated its healing. The asymmetric JHA comprised a mechanical supporting layer (SL) hydrogel and a newly formed repairing layer (RL) hydrogel, which was in situ growing on the tissue surface initiated by the catalytic reaction of blood glucose and GOx/Fe[Gly]₂ at the interface of SL. Accordingly, the blood and water on the wound surface were self-entrapped as components within the in-situ formed RL to mitigate their negative impact on the wet interface, ensuring effective contact between the tissue and the hydrogel adhesive. Meanwhile, the

formation of covalent bonds with tissue surface via NHS-amino reaction facilitates enhanced interfacial interaction during the in-situ gelation process, resulting strong wet-adhesion for seamless fistula plugging. In addition, the asymmetric JHA with effective interlocking effect could dissipate energy to tolerate the external forces caused by physiological activities like chewing and swallowing, leading to long-term dynamic mechanical adaptability. This approach overcomes the limitations of conventional hydrogel adhesives which are often performed with compromised mechanical properties and therapeutic benefits, offering a promising solution to address the clinical challenges in leak-related tissue sealing and healing.

The mechanical and sealing properties of the designed JHA were also comprehensively evaluated *in vitro* and *in vivo*. It was found that the SL hydrogel exhibited excellent mechanical stability and ability to withstand external forces, which may attribute to the tough three-dimensional polymer network and the multiple noncovalent interactions between polyacrylic acid and polysaccharide, enabling effective energy dissipation in the deformation process. The opposite side RL hydrogel was *in situ* growing on the surface of SL and tissue via the SEIP process, thus creating a seamless adhesion to fistula. Both interfacial toughness and shear strength tests under different conditions suggested the strong and stable adhesive properties of JHA, superior to currently available commercial tissue adhesives. In addition, the sealing performance was also verified in New Zealand rabbit and Beagle POF models, demonstrating a tight adhesion to the mucosal defect for more than 3 days without any sign of decreased adhesion, as well as excellent fluid-tight sealing without water seeping or flowing out, proving the effectiveness of the SEIP approach.

Importantly, compared to currently existing hydrogel adhesives, the developed JHA is capable of regulating the biochemical micro-environment based on enzymatic reactions of the encapsulated GOx/Fe[Gly]₂ and blood glucose. *In vitro* experiments showed that the JHA can effectively prevent bacterial growth, reduce ROS and inflammation to improve metabolic processes, and stimulate the polarization of macrophage phenotypic from M1 to M2, thereby inducing cells proliferation and differentiation. Continued studies both in New Zealand rabbit and beagle dog models also demonstrated the feasibility of the designed JHA for POFs sealing and supporting the healing process. Despite its early developmental stage, the JHA offers promising commercial potential to POF defect repair, and provides an opportunity for the repair of other complex yet dynamic penetrating injuries in the human body.

Although the current work provides an important attempt to develop a promising hydrogel adhesive for fistula sealing and repair, there are still several limitations and issues that need to be addressed before future clinical applications. The biodegradation rate of the hydrogel should be precisely tailored to harmonize with the fistula healing process, and an implantable biological patch can replace the SL layer, thereby minimizing the risk of long-term foreign body retention. Benign detachment on demand is also critical to avoid causing secondary damage. Further loading and responsive release of therapeutics and drugs (such as growth factors) within the hydrogel would be desirable to accelerate the fistula healing process. In addition, it is imperative to comprehensively consider the storing stability, operational convenience, and experience comfort to accommodate the varying demands of patients.

Methods

Preparation of Janus hydrogel adhesive

Supporting layer (SL) hydrogel: Dissolve 30% (w/w) acrylic acid, 6% (w/w) chondroitin sulfate, and 4% (w/w) CSMA in deionized water, and add 1% α -ketoglutaric acid as an initiator. Adjust the pH value to 5.5–6 with 10 M NaOH solution, vortex and shake to form a uniform precursor solution. The precursor solution was added to a glass mold with a 1 mm thick silicone gasket, cured under ultraviolet light (365 nm, 22.4 mW/cm²) for

20 min, and freeze-dried. Finally, it is sealed in a plastic bag containing a desiccant and stored at –20 °C before used.

Repairing layer (RL) hydrogel precursor solution: Add 8% (w/w) CSMA, 2% (w/w) DMAA, 1.25% (w/w) AAc-NHS, glucose (0.5 mg/mL), Fe[Gly]₂ (0.2 mg/mL) into deionized water, vortex and shake to form a uniform precursor fluid.

When in use, the completely dried SL hydrogel was coated with GOx (100 U/mL) solution, subsequently, proper amount of RL precursor solution was applied to its surface and form RL hydrogel through enzymatic polymerization. As a result, one kind of *in-situ* Janus hydrogel adhesive (JHA) is well prepared.

Material characterizations

The ¹H NMR spectra of methacrylated chondroitin sulfate were acquired on a Bruker AVANCE III HD 600 MHz NMR spectrometer. Mechanical properties of the hydrogel were tested by the electronic universal testing machine (UTM 2502, Shenzhen Sun Technology StockCO., LTD.). The measurement speed of the compression test was 2 mm/min, the sample diameter was 14 mm, and the thickness was 6–8 mm. The modulus of the hydrogel was calculated using stress and strain data with a strain of 5–15%. The tensile test measurement speed was 20 mm/min, and the samples were rectangular, with width of 1 cm and thickness of 1 mm. The puncture measurement was conducted using a traction needle with a diameter of 2 mm and a length of 7 cm, applied at a speed of 10 mm/min.

Rheological Measurements were performed to determine the gelation time and mechanical stability of the hydrogel, using a Thermo Haake rheometer (RS6000, Thermo Scientific, USA) to measure the storage modulus (*G'*) and loss modulus (*G''*) of the hydrogel at a frequency of 1 Hz and shear stress 1 Pa. Dynamic time sweeps were executed using a parallel plate geometry (diameter: 20 mm, 0.3 mm gap) at 37 °C for 3600 s, after which a dynamic frequency sweep of 10–0.1 Hz was performed on the hydrogel.

SEM were used to observe the microscopic structures of JHA and AFM was used to observe the roughness of JHA before and after RL formed at the interface of SL. The prepared JHA was frozen in liquid nitrogen and subsequently undergo drying in a freeze dryer for a duration of 72 h for SEM test. Following this, it was sprayed with gold using a current intensity of 15 mA for 2 min, then a field emission scanning electron microscope (S-4800, Hitachi, Japan) was used to observe the cross-section structure of the hydrogel, with a working voltage of 5 kV.

Adhesive property test

All adhesion performance tests were carried out by electronic universal testing machine (UTM 2502, Shenzhen Sun Technology StockCO., LTD.). To simulate the moist environment in the body, the biological tissues such as porcine skin were first soaked in PBS (pH = 7.4), and then used directly without drying, to test the adhesion performance of the hydrogel to biological tissues in a moist environment.

To measure the interfacial toughness, a 180° peel test was carried out according to ASTM F2256 at a constant speed of 50 mm/min. The length of the hydrogel used for adhesion was 4 cm and the width was 2.5 cm. The calculation formula of interfacial toughness is as follows:

$$\text{Interfacial toughness} = \frac{2 \times F_{\text{plateau}}}{w_1} \quad (1)$$

where *F*_{plateau} represents the plateau force during peeling, and *w*₁ denotes the width of the adhesion area. All the tests were conducted in triplicate for each group.

To measure the shear strength, the lap-shear test was carried out according to ASTM F2255 at a constant speed of 50 mm/min. The length of the hydrogel used for adhesion was 1 cm and the width was

2.5 cm. The shear strength calculation formula is as follows:

$$\text{Shear strength} = \frac{F_{\max}}{w_2 \times l_2} \quad (2)$$

where F_{\max} refers to the maximum force during shearing, while w_2 and l_2 represent the width and length of the adhesion area, respectively.

Antibacterial activity

In order to simulate the antibacterial effect of the hydrogel adhesive in human blood glucose environment, Nutrient-Broth (NB) medium containing 6.1 mM glucose was prepared in advance: After the glucose solution and the NB medium were sterilized separately, an appropriate amount of glucose solution was added to the NB medium, the final concentration of glucose is 6.1 mM (human fasting blood glucose content is 3.9 ~ 6.1 mM).

Inhibition zone test: 20 μ L bacterial suspension (10^6 CFU/mL) was taken and transferred to the NB agar plate, then spread evenly with a sterile spatula immediately, and dried at room temperature for 2 min. After sterilization, SL and JHA hydrogels with a diameter of 5 mm were placed in the middle of the plates containing the bacterial solution, and the samples were gently pressed with sterile tweezers to make them close to the surface of the plate. After the Petri dishes were cultured upside down in a constant temperature incubator at 37 °C for 24 h, the sizes of the inhibition zone were measured to evaluate the antibacterial performance of the samples.

In order to test the continuous antibacterial effect of the hydrogel, the cultured hydrogels were transferred to new NB agar plates coated with bacterial solution every 24 h, and the procedure was repeated until the inhibition zone disappeared to test the antibacterial persistence of hydrogel adhesive.

Inhibition rate test: 200 μ L bacterial suspension (10^8 CFU/mL) was added to 40 mL NB medium, and then 1.5 g JHA hydrogel was immersed in the medium as experimental group. The medium containing only bacterial solution was used as POF-only group, and the NB medium was used as background group to correct the zero point. After being cultured for 24 h in a constant temperature shaker at 37 °C, an appropriate amount of bacterial solution was taken to measure the absorbance at 600 nm to characterize the bacterial solution turbidity. The calculation formula of antibacterial rate is as follows:

$$\text{Antibacterial rate} = \frac{A_0 - A_1}{A_0} \times 100\% \quad (3)$$

where A_0 , A_1 represent the absorbance of POF-only control group and sample group respectively.

For *in vivo* bacterial analysis, the orocutaneous wound of an experimental rabbit was firstly cleansed with physiologic saline. A sterile swab was then applied on the wound via gently rotating and scraping around its surface. After specimen collection, the swab was placed in a transport medium and sent to the Microbiology Laboratory for further culture analysis. Then, each swab was plated onto two media: blood agar, McConkey agar. The growth of bacteria might be found by morphologic changes of the colonies after incubation of media for 24 h. The colonies were then sent for biochemical identification using the automated Vitek COMPACT system (bioMérieux, Marcy l'Etoile, France). These procedures followed the manufacturer's recommendations.

In vitro cell studies

We used the CCK-8 kit to detect the RL precursor solution (8% (w/w) CSMA, 2% (w/w) DMAA, 0.5 mg/mL Fe[Gly]₂), SL and JHA powder dispersion (1 g powder is soaked in 10 ml DMEM medium at 37 °C for 24 h) to verify their cytotoxicity. L929 cells (NCTC clone 929, SCSP-5039,

CSTR:19375.09.3101MOUSCSP5039) were seeded with 100 μ L/well cell suspension in 96-well plates at a density of 6×10^3 /well and 4×10^3 /well, respectively. The culture plates were placed in the constant temperature incubator at 37 °C and 5% CO₂ for 24 h, then the culture medium was removed. Different concentrations of RL precursor, SL and JHA hydrogel powder dispersion were added to DMEM to co-cultivate for 24 h and 48 h (37 °C, 5% CO₂). After removing the medium again, 100 μ L of DMEM medium (containing 10 μ L CCK-8) was added to each well and incubated for 45 min. Relative cell survival rate was calculated by measuring the absorbance at 450 nm with a microplate reader (ELx 808 IU, BioTek, USA). This group of experiments was set up with three groups of parallel experiments, and the cells cultured in the whole medium were used as control groups.

In order to further verify the biocompatibility of the gel-forming system, we performed live/dead cell assay to reflect cell viability. Extracted solution of RL hydrogel (final concentration of 2 mg/mL) and SL and JHA hydrogel powder dispersion (final concentration of 0.1 mg/mL) were prepared in the same way as cell proliferation and toxicity tests. NIH 3T3 and L929 were seeded in 48-well plates with 300 μ L/well cell suspension at a density of 1.2×10^4 /well and 1.0×10^4 /well. After the culture plates were placed in the constant temperature incubator at 37 °C and 5% CO₂ for 24 h, the culture solution was removed, 300 μ L RL precursor and SL and JHA hydrogel powder dispersion were added to culture for 24 h. Then the culture medium was removed again, 300 μ L Calcein AM/PI staining reagent (AM: 4 μ M, PI: 4.5 μ M) was added to each well, stained for 15 min, and washed twice. Fluorescence microscope (DM2500, Leica) was used for imaging to observe live cells (green fluorescence) and dead cells (red fluorescence).

The intracellular ROS scavenging ability of the RL hydrogel was investigated using DCFH-DA as the fluorescent probe. Hydrogels with 0.2 mg/mL, 0.5 mg/mL and 1 mg/mL Fe[Gly]₂ were prepared in advance. After L929 cells were seeded in 48-well plates at a density of 1.2×10^4 /well and 1.0×10^4 /well and cultured for 24 h, they were incubated with the following materials: (1) 10 μ L PBS as control; (2) 10 μ L H₂O₂ (final concentration 100 μ M); (3) 10 μ L H₂O₂ and 100 μ g SL hydrogel containing 0.2 mg/mL Fe[Gly]₂; (4) 10 μ L H₂O₂ and 100 μ g RL hydrogel containing 0.2 mg/mL Fe[Gly]₂; (5) 10 μ L H₂O₂ and 100 μ g RL hydrogel containing 0.5 mg/mL Fe[Gly]₂; (6) 10 μ L H₂O₂ and 100 μ g hydrogel containing 1 mg/mL Fe[Gly]₂. After being incubated in the constant temperature incubator at 37 °C and 5% CO₂ for 2 h, the cells were incubated in DCFH-DA (5 μ M in DMEM, without FBS) for 20 min, and gently washed with PBS three times. Finally, a fluorescence microscope was used to detect the green fluorescence in the cell to assess the ROS levels in the cells (DM2500, Leica).

To further evaluate the anti-inflammatory activity and immunomodulatory properties of the RL hydrogels, 1.0×10^5 RAW 264.7 cells were seeded in a 24-well plate and cultured overnight, and then the cells were treated with or without 1 μ g/mL LPS for 24 h. Subsequently, 1 μ g LPS was added to each well, and the cells were cultured for 24 h. Then the cells were treated with or without 1 μ g/mL LPS for 24 h. Next, the cells were fixed with 4% paraformaldehyde for 15 min, permeabilized with 0.2% (v/v) Triton X-100 for 15 min and blocked with a 10% BSA solution. The cells were then incubated with anti-IL-6 antibody ([EPR16610-69] (ab179570), abcam, 1:100)/FITC labeled goat anti-rabbit IgG (H + L) (1:500; A0562, Beyotime, China), Anti-TNF- α antibody ([52B83] ab1793, 1:200)/Cy3 labeled goat anti-mouse IgG (H + L) (1:500; A0521, Beyotime, China), abcam, and iNOS (D6B6S) Rabbit mAb (Alexa Fluor® 488 Conjugate) (93421, 1:200)/CoraLite®594-conjugated CD206 Monoclonal antibody (CL594-60143, 1:50) respectively. Nuclei were counterstained with DAPI and cells were thoroughly washed with PBS before observation. Fluorescent images were captured using a confocal microscopy (Olympus, FV1000). All studies were performed in triplicate.

Animal experiments

All procedures for the *in vivo* animal studies were performed in the animal labs at Jiagan Biotechnology Co. Shanghai (JBS), all the animal surgeries and perioperative protocols were carried out in complete compliance with the Animal Research Care and Ethical Regulations approved by the Ethical Committee on Animal Care of Shanghai 9th People's Hospital, affiliated to Shanghai Jiao Tong University (No. SH9H-2021-A331).

In vivo evaluation in New Zealand rabbit models

Forty-five New Zealand White male rabbits, ~16 weeks of age (2.8–3.5 kg), were randomly divided into 3 groups (POF-only group, Idioform group and experimental group JHA hydrogel) in the present study. Prior to anesthesia, rabbits' weight was measured, and the blood samples were collected for analyses of hematological parameters. The premedication of rabbit was done with ketamine 5 mg/kg, xylazine 4 mg/kg via muscular injection and buprenorphine 0.04 mg/kg via marginal ear vein. After sedation, the anesthesia was maintained with 1% isoflurane via pure-oxygen facemask with a respiratory monitor. Warm surgical scrub and continuous administration of warm NaCl 0.9% 5 mL/kg/h were used to avoid hypothermia during the procedures. Penicillin 100,000 IU/mL were administered before surgery.

The left buccal area was shaved and sterilized, an oval incision of 1.5 cm × 2 cm was planned for each rabbit. The anatomic location for the incision line was in the middle region between the anterior border of masseter muscle and the posterior border of canines. Such design was to avoid the accidental incision of facial arteries or vein, resulting in excessive intraoperative bleeding or postoperative hematoma. After incision, a through-and-through orocutaneous defect (from skin to mucosa) was prepared for *in vivo* assessment of the JHA's sealing and repairing capabilities. The orocutaneous defects were repaired with three different treatment modalities (groups): (1) POF-only group (control); (2) Idioform group; (3) JHA hydrogel. Antiseptic idioform gauze was clinically used for defect space-filling while hydrogel was the material we used for tests. To ensure minimal tissue damage, Iodoform was folded into a Vaseline gauze, and then the idioform gauze was fixed and packed with retention stitches, while hydrogel was placed in the inner rim around the mucosal layer of the defect. The idioform gauze was changed every 4 days postoperatively under general anesthesia, while the other two groups were treated with simple wound cleansing and debridement. For each group, nine rabbits were surgically treated. In all cases, rabbits were closely monitored for recovery, weight loss and food consumption postoperatively. For the sake of pain relief, meloxicam (0.3 mg/kg) was administered once a day for the first 3 days following surgery. Besides, postoperatively, for each rabbit, 3 days of antibiotic prophylaxis by intravenous injection of amoxicillin-clavulanate 7.5 mg/kg per day was carried out due to possible buccal wound contamination of oral intake and food-saliva disturbance. Three rabbits in each group were euthanized on days 4, 8, and 12 postoperatively. Before euthanasia, wound recovery was macroscopically observed, and blood samples were obtained for further analyses. After euthanasia, the harvested specimens were analyzed histologically.

In vivo repairing evaluation in Beagle dog models

With the aforementioned ethics approval, a total of nine purpose-bred healthy male beagles (3.5–4 years of age), weighing between 9 and 14 kg, were enrolled and randomly divided into 3 groups (POF-only group, Idioform group and JHA group). As welfare of research, all dogs were housed individually. Before treatment, they were fasted for 8 h. Following intramuscular administration with atropine sulfate (0.05 mg/kg) and morphine sulfate (0.8 mg/kg), an intravenous catheter was placed and anesthesia was induced with propofol (6 mg/kg). With endotracheal intubation for keeping airway patent,

anesthesia was maintained with isoflurane (2% delivered in oxygen 30 ml/kg/min). Prewarmed Lactated Ringer's Solution (10 ml/kg/h) was administered during anesthesia. The body was covered with warmed surgical scrub, while the buccal region was disinfected.

Similar to the surgical treatment in rabbit, a 3 × 2.5 cm buccal incision for through-and-through orocutaneous defect was planned in the middle 1/3 of the facial region. All the experimental dogs were allocated into three groups in terms of different treatment of the wounds: (1) POF-only group; (2) Idioform group; (3) JHA hydrogel. For welfare of animals, morphine sulfate (1 mg/kg) was administered every 6–8 h as needed during the first operative day. Besides, postoperatively, 5 days of antibiotic prophylaxis by intravenous injection of amoxicillin-clavulanate 10 mg/kg per day was applied in all these dogs. Because dogs often use flexible tongue to lick wounds, which is easy to damage the JHA and suture Idioform gauzes. Therefore, JHA and Iodoform gauzes were changed regularly until the wound is healed. JHA was replaced on day 4 and day 8, and Idioform gauzes were replaced on the day 4, day 8, and day 12 postoperative day under general anesthesia, while others were anesthetized for wound cleansing and debridement. In addition, clinical measurements were taken on Day 0, 4, 8, 12, 17, and 22. All were euthanized on Day 22 and specimens were collected for analyses.

Clinical evaluation of wounds

The buccal wounds were measured for both rabbits and dogs on the day of dressing changes or euthanasia. Fine-resolution digital image of every wound was taken with a metric measurement scale placed at level with the wound surface. Total buccal cutaneous wound areas were compared for ease of observation. On day of euthanasia, the wound was horizontally resected open for view of the inner wound recovery. Before euthanasia, bacterial culture was also taken for analysis between the groups.

Hematologic parameters

Hematological analysis was performed at the Shanghai 9th People's Hospital laboratory using Beckman Coulter: AU 480 Chemistry System. The analyzed hematological parameters included: red blood cell (RBC) count, hemoglobin (Hgb), total white blood cell (WBC) count, differential WBC count (percentage of neutrophils). These were to reflect the changes of both the nutritional and inflammatory conditions. Besides, liver and kidney functions, regarding alanine transaminase (ALT), aspartate aminotransferase (AST), glutamyl transferase (GGT), creatinine (CREA), and blood urea nitrogen (BUN) were compared between the groups.

Histologic analyses (Hematoxylin-eosin and Masson's Trichrome staining)

Specimens were collected *en bloc* and fixed in 10% buffered formalin for at least 24 h before being embedded in paraffin. Sections (4 μm) were firstly obtained and stained with hematoxylin-eosin (H&E) and Masson's Trichrome staining. All samples were examined microscopically by a board-certified pathologist who was blinded to the sample status. After identifying the dermal and mucosal sides, specific measurements were taken to evaluate the following four endpoints: epithelialization, mucosal epithelial integrity and inflammation.

Immunohistochemical analysis

Sections from selected paraffin blocks for each specimen were used for immunohistochemical analysis. The antigen retrieval process was performed an EDTA citrate buffer (pH 8.3) for 30 min, followed by detection with the ultraView Universal DAB Detection Kit on the Ventana Roche System. For specimens of rabbits, anti-α-SMA antibody, 1:100 dilution, 20 min incubation, for the staining of myofibroblasts, anti-CD31, 1:300 dilution for the staining of vascular or neovascular cells. Anti-IL-6, 1:400 dilution was used for the staining of lymphocytes

and neutrophils. Anti-PCNA 1:1000 dilution, Anti-8-OHdG 1:200 (bs-1278R, Bioss) and anti-4-HNE (bs-6313R, Bioss) 1:25 were used for evaluation of the oxidative stress at wound site. CD68, 1:200 dilution (gb11067, Seville) and CD206, 1:200 dilution (ab64693, Abcam) was used for evaluation of the inflammation levels at the wound sites. As for canine specimens, the antibodies dilutions were as follows: anti- α -SMA (1:1000), anti-IL-6 (1:200) and anti-CD31 (1:300). The staining intensity were compared between different groups.

Statistics and reproducibility

All statistical data are presented as means \pm standard deviations (SD) and were performed with GraphPad Prism 8 (GraphPad, USA). Two-tailed Student's *t* test was for comparison between two groups and one-way analysis of variance (ANOVA) with Tukey's multiple comparisons test was used for multiple-group comparisons. All experiments were repeated independently with similar results at least three times. A $p < 0.05$ was considered statistically significant.

Reporting summary

Further information on research design is available in the Nature Portfolio Reporting Summary linked to this article.

Data availability

The data supporting the findings of this study are available within the paper and its supplementary information. Any additional requests for information can be directed to and will be fulfilled by the corresponding authors. Source data are provided with this paper.

References

- Toma, A. I., Fuller, J. M., Willett, N. J. & Goudy, S. L. Oral wound healing models and emerging regenerative therapies. *Transl. Res.* **236**, 17–34 (2021).
- Kwon, D. et al. Overcoming wound complications in head and neck salvage surgery. *Auris Nasus Larynx* **45**, 1135–1142 (2018).
- Bigliardi, P. L. et al. Povidone iodine in wound healing: a review of current concepts and practices. *Int. J. Surg.* **44**, 260–268 (2017).
- Hao, X. & Lv, K. Iodoform Gauze Packing is an Alternative Therapy for Postoperative Parotid Fistula. *J. Craniofac. Surg.* **34**, 755–756 (2023).
- Inatomi, Y. et al. Utility of negative-pressure wound therapy for orocutaneous and pharyngocutaneous fistula following head and neck surgery. *Head Neck* **42**, 103–110 (2020).
- Okazaki, M. et al. Analysis of salvage treatments following the failure of free flap transfer caused by vascular thrombosis in reconstruction for head and neck cancer. *Plast. Reconstr. Surg.* **119**, 1223–1232 (2007).
- Cui, C. et al. A self-stabilized and water-responsive deliverable coenzyme-based polymer binary elastomer adhesive patch for treating oral ulcer. *Nat. Commun.* **14**, 7707 (2023).
- Zhao, X. A bioadhesive robot to activate muscles. *Nat. Mater.* **22**, 149–150 (2023).
- Wang, H. et al. A super tough, rapidly biodegradable, ultrafast hemostatic bioglue. *Adv. Mater.* **35**, 2208622 (2023).
- He, Y. et al. A smart adhesive Janus hydrogel for non-invasive cardiac repair and tissue adhesion prevention. *Nat. Commun.* **13**, 7666 (2022).
- Wu, S. J. & Zhao, X. Bioadhesive technology platforms. *Chem. Rev.* **123**, 14084–14118 (2023).
- Fan, H. & Gong, J. P. Bioinspired underwater adhesives. *Adv. Mater.* **33**, 2102983 (2021).
- Zhao, Y. et al. Supramolecular adhesive hydrogels for tissue engineering applications. *Chem. Rev.* **122**, 5604–5640 (2022).
- Yuk, H. et al. Dry double-sided tape for adhesion of wet tissues and devices. *Nature* **575**, 169–174 (2019).
- Wang, Z., Guo, L., Xiao, H., Cong, H. & Wang, S. A reversible underwater glue based on photo- and thermo-responsive dynamic covalent bonds. *Mater. Horiz.* **7**, 282–288 (2020).
- Pan, F. et al. Hydrogel networks as underwater contact adhesives for different surfaces. *Mater. Horiz.* **7**, 2063–2070 (2020).
- Cui, C. et al. Water-triggered hyperbranched polymer universal adhesives: from strong underwater adhesion to rapid sealing hemostasis. *Adv. Mater.* **31**, 1905761 (2019).
- Epstein, A. K., Wong, T.-S., Belisle, R. A., Boggs, E. M. & Aizenberg, J. Liquid-infused structured surfaces with exceptional anti-biofouling performance. *Proc. Natl. Acad. Sci. USA* **109**, 13182–13187 (2012).
- Wu, S. J., Yuk, H., Wu, J., Nabzdyk, C. S. & Zhao, X. A multifunctional origami patch for minimally invasive tissue sealing. *Adv. Mater.* **33**, 2007667 (2021).
- Freedman, B. R. et al. Enhanced tendon healing by a tough hydrogel with an adhesive side and high drug-loading capacity. *Nat. Biomed. Eng.* **6**, 1167–1179 (2022).
- Cui, C. et al. A Janus hydrogel wet adhesive for internal tissue repair and anti-postoperative adhesion. *Adv. Funct. Mater.* **30**, 2005689 (2020).
- Zhang, Y. et al. Successive redox-reaction-triggered interface radical polymerization for growing hydrogel coatings on diverse substrates. *Angew. Chem. Int. Ed.* **61**, e202209741 (2022).
- Zhang, Q. et al. Tissue fluid triggered enzyme polymerization for ultrafast gelation and cartilage repair. *Angew. Chem. Int. Ed.* **60**, 19982–19987 (2021).
- Liao, Y., Wang, X., Shen, H., Tai, Z. & Wang, Q. Dynamic assembly and biocatalysis-selected gelation endow self-compartmentalized multienzyme superactivity. *Sci. Chin. Chem.* **65**, 1985–1993 (2022).
- Wang, X. & Wang, Q. Enzyme-laden bioactive hydrogel for biocatalytic monitoring and regulation. *Acc. Chem. Res.* **54**, 1274–1287 (2021).
- Ji, J., Joh, H.-I., Chung, Y. & Kwon, Y. Glucose oxidase and polyacrylic acid based water swellable enzyme-polymer conjugates for promoting glucose detection. *Nanoscale* **9**, 15998–16004 (2017).
- Li, M., Blum, N. T., Wu, J., Lin, J. & Huang, P. Weaving enzymes with polymeric shells for biomedical applications. *Adv. Mater.* **33**, 2008438 (2021).
- He, X. et al. A compartmentalized nanoreactor formed by interfacial hydrogelation for cascade enzyme catalytic therapy. *Angew. Chem. Int. Ed.* **62**, e202218766 (2023).
- Wu, Y. et al. A smart indwelling needle with on-demand switchable anticoagulant and hemostatic activities. *Mater. Horiz.* **7**, 1091–1100 (2020).
- Liang, W. et al. Peritoneum-inspired Janus porous hydrogel with anti-deformation, anti-adhesion, and pro-healing characteristics for abdominal wall defect treatment. *Adv. Mater.* **34**, 2108992 (2022).
- Saraswathibhatla, A., Indana, D. & Chaudhuri, O. Cell-extracellular matrix mechanotransduction in 3D. *Nat. Rev. Mol. Cell Biol.* **24**, 495–516 (2023).
- Taboada, G. M. et al. Overcoming the translational barriers of tissue adhesives. *Nat. Rev. Mater.* **5**, 310–329 (2020).
- Chen, K., Wu, Z., Liu, Y., Yuan, Y. & Liu, C. Injectable double-crosslinked adhesive hydrogels with high mechanical resilience and effective energy dissipation for joint wound treatment. *Adv. Funct. Mater.* **32**, 2109687 (2022).
- Fil, D., Borysiewicz, E. & Konat, G. W. A broad upregulation of cerebral chemokine genes by peripherally-generated inflammatory mediators. *Metab. Brain Dis.* **26**, 49–59 (2011).
- Hu, X., Li, J., Fu, M., Zhao, X. & Wang, W. The JAK/STAT signaling pathway: from bench to clinic. *Signal Transduct. Target. Ther.* **6**, 402 (2021).
- O'Shea, John J. & Plenge, R. JAK and STAT signaling molecules in immunoregulation and immune-mediated disease. *Immunity* **36**, 542–550 (2012).

37. Miklossy, G., Hilliard, T. S. & Turkson, J. Therapeutic modulators of STAT signalling for human diseases. *Nat. Rev. Drug Discov.* **12**, 611–629 (2013).
38. Villarino, A. V., Kanno, Y. & O’Shea, J. J. Mechanisms and consequences of Jak–STAT signaling in the immune system. *Nat. Immunol.* **18**, 374–384 (2017).
39. Nakamoto, N. et al. CCR9+ macrophages are required for acute liver inflammation in mouse models of hepatitis. *Gastroenterology* **142**, 366–376 (2012).
40. Miyabe, Y., Lian, J., Miyabe, C. & Luster, A. D. Chemokines in rheumatic diseases: pathogenic role and therapeutic implications. *Nat. Rev. Rheumatol.* **15**, 731–746 (2019).
41. Yokoyama, W. et al. Abrogation of CC chemokine receptor 9 ameliorates collagen-induced arthritis of mice. *Arthritis Res. Ther.* **16**, 445 (2014).
42. Britton, G. J. et al. Microbiotas from humans with inflammatory bowel disease alter the balance of Gut Th17 and ROR γ t(+) regulatory T cells and exacerbate colitis in mice. *Immunity* **50**, 212–224.e214 (2019).
43. Hovhannisyan, Z., Treatman, J., Littman, D. R. & Mayer, L. Characterization of interleukin-17-producing regulatory T cells in inflamed intestinal mucosa from patients with inflammatory bowel diseases. *Gastroenterology* **140**, 957–965 (2011).
44. Majumder, S. et al. IL-17 metabolically reprograms activated fibroblastic reticular cells for proliferation and survival. *Nat. Immunol.* **20**, 534–545 (2019).
45. Mills, K. H. G. IL-17 and IL-17-producing cells in protection versus pathology. *Nat. Rev. Immunol.* **23**, 38–54 (2023).
46. Li, X., Bechara, R., Zhao, J., McGeachy, M. J. & Gaffen, S. L. IL-17 receptor-based signaling and implications for disease. *Nat. Immunol.* **20**, 1594–1602 (2019).

Acknowledgements

This work was supported by the National Key Research and Development Program of China (No. 2022YFC2403200, to Q.G.W.), the National Science Fund for Distinguished Young Scholars (No. 52125305, to Q.G.W.), the National Natural Science Foundation of China for Excellent Youth Scholars (T2322022, to X.W.), the National Natural Science Foundation of China (No. 52173289, to X.W.; 52273147, to D.W.), Hainan Province Clinical Medical Center, Hainan Provincial Natural Science Foundation of China, Cross-disciplinary Research Fund of Shanghai Ninth People’s Hospital (JYJC202314, to C.M.), Shanghai JiaoTong university School of Medicine, Natural Sciences Fund in Hainan Province (SQ2024MSXM0324, to C.M.). We thank Zonghui ZHAO in Shanghai Fourth People’s Hospital for his help with the materials preparation and Ronghui XIA in Shanghai Ninth People’s Hospital for his help with the histological assessments.

Author contributions

Q.G.W., X.Q., Q.W., X.W., Y.J., L.D., C.M., D.W., M.S. conceived and design the research. Y.J. and L.D. conducted the preparation, characterization, and data analysis of the JHA, as well as the in vitro and ex vivo experiments. Y.J., L.D., and C.M. performed the in vivo experiments. Y.J., L.D., C.M., Q.W., D.W., and M.S. co-wrote the manuscript with input from all authors. Q.G.W. and Q.W. supervised the study. All authors edited the manuscript and approved the final version.

Competing interests

The authors declare no competing interests.

Additional information

Supplementary information The online version contains supplementary material available at <https://doi.org/10.1038/s41467-024-55303-w>.

Correspondence and requests for materials should be addressed to Qing Wu, Xingjun Qin or Qigang Wang.

Peer review information *Nature Communications* thanks the anonymous reviewers for their contribution to the peer review of this work.

Reprints and permissions information is available at <http://www.nature.com/reprints>

Publisher’s note Springer Nature remains neutral with regard to jurisdictional claims in published maps and institutional affiliations.

Open Access This article is licensed under a Creative Commons Attribution-NonCommercial-NoDerivatives 4.0 International License, which permits any non-commercial use, sharing, distribution and reproduction in any medium or format, as long as you give appropriate credit to the original author(s) and the source, provide a link to the Creative Commons licence, and indicate if you modified the licensed material. You do not have permission under this licence to share adapted material derived from this article or parts of it. The images or other third party material in this article are included in the article’s Creative Commons licence, unless indicated otherwise in a credit line to the material. If material is not included in the article’s Creative Commons licence and your intended use is not permitted by statutory regulation or exceeds the permitted use, you will need to obtain permission directly from the copyright holder. To view a copy of this licence, visit <http://creativecommons.org/licenses/by-nc-nd/4.0/>.

© The Author(s) 2024